RSC Advances

PAPER

View Article Online
View Journal | View Issue

Cite this: *RSC Adv.*, 2024, **14**, 23152

Design, synthesis and characterization of tetra substituted 2,3-dihydrothiazole derivatives as DNA and BSA targeting agents: advantages of the visible-light-induced multicomponent approach†

Ranjana Aggarwal, *[ab] Naman Jain[a] and Gyan Prakash Dubey[a]

This report describes the visible-light-induced one-pot multicomponent regioselective synthesis of a series of 5-aroyl-3-((arylidene)amino)-2-((arylidene)hydrazono)-4-methyl-2,3-dihydrothiazoles as DNA and BSA targeting agents. The multicomponent condensation of thiocarbohydrazide and aldehydes with α-bromo-1,3-diketones, generated *in situ* by the bromination of unsymmetrical 1,3-diketones with NBS using white LED light as an environmental friendly source in the presence of EtOAc solvent furnished the titled 2,3-dihydrothiazole derivatives in excellent yields. The exact regioisomeric structure was identified unambiguously by employing multinuclear 2D-NMR spectroscopy [^{1}H–^{13}C] HMBC; [^{1}H–^{13}C] HMQC and [^{1}H–^{15}N] HMBC. Furthermore, the binding characteristics of the synthesized 2,3-dihydrothiazole derivatives were assessed with double-stranded calf-thymus DNA duplex (ct-DNA) and bovine serum albumin (BSA). Initial screening of all the synthesized 2,3-dihydrothiazole derivatives using various *in silico* techniques including molecular reactivity analysis, Lipinski rule and molecular docking, concluded 5-(4′-chlorobenzoyl)-3-((4″-methoxybenzylidene)amino)-2-(4‴-methoxybenzylidene)hydrazono)-4-methyl-2,3-dihydrothiazole derivative **6a** as the most suitable compound for studying binding interaction with DNA and BSA. Additionally, to illustrate the *ex vivo* binding mode of **6a** with DNA and BSA, several spectroscopic techniques *viz.* UV-visible, circular dichroism (CD), steady-state fluorescence and competitive displacement assays were carried out.

Received 27th March 2024
Accepted 22nd June 2024

DOI: 10.1039/d4ra02331e

rsc.li/rsc-advances

1. Introduction

Among the current research on mainstream azoles, the heteroaromatic thiazole nucleus gained extensive appreciation in drug development as a result of its fascinating implication in pharmaceuticals. The presence of N and S atoms enables the thiazole ring to interact with various biological receptors and help it to impart its therapeutic effect.[1] As a consequence, the thiazole ring exhibits tremendous biological and chemotherapeutic significance such as anticancer,[2] anti-inflammatory,[3] anthelmintic,[4] analgesic,[5] antimicrobial,[6] anti-HIV,[7] antioxidant,[8] antimalarial,[9] antibiotic[10] *etc.* Thiazole core also signifies its importance in various naturally occurring bioactive compounds such as Thiamin,[11] Thiamine pyrophosphate,[12] Epothilone,[13] Mycothiazole[14] *etc.* Apart from this, the thiazole core marks its prominence in other fields of science as well for instance as polymers, photosensitizers, semiconductors, fluorescent dyes, and dye-sensitized solar cells.

Deoxyribonucleic acid (DNA) is one of the most important biomacromolecules as it contains the genetic information that controls the growth of almost all living organisms.[15,16] Any modification in the basic functioning of DNA molecules may cause several types of diseases in the human body namely cystic fibrosis, sickle cell disease, genetic disorders, Huntington's disease *etc.* Recent research has revealed that the thiazole ring can preferentially interact with DNA, altering its functioning and thus being used to treat nucleic acid-dependent diseases. The small organic molecules can interact with DNA through non-covalent bonding mainly following one of the three possible mechanisms: intercalation, groove binding and electronic interactions.[17] Thus, researchers have shifted their efforts to the design and synthesis of novel thiazole derivatives that can target the DNA molecule. Fig. 1 comprises the rationale drug designing of molecule under consideration and thiazole core-

[a]*Department of Chemistry, Kurukshetra University, Kurukshetra 136119, Haryana, India*

[b]*CSIR-National Institute of Science Communication and Policy Research, New Delhi 110012, India. E-mail: ranjana67in@yahoo.com; ranjanaaggarwal67@gmail.com; Tel: +91-9896740740*

† Electronic supplementary information (ESI) available: The ESI consists of additional experimental data, (^{1}H, ^{13}C, [^{1}H–^{13}C] HMBC; [^{1}H–^{13}C] HMQC and [^{1}H–^{15}N] HMBC) for final compounds, Van't Hoff plot, CD spectrum for DNA, fluorescence spectra of BSA-IB and BSA-PB complex and general experimental section for both synthesis and binding studies. See DOI: https://doi.org/10.1039/d4ra02331e

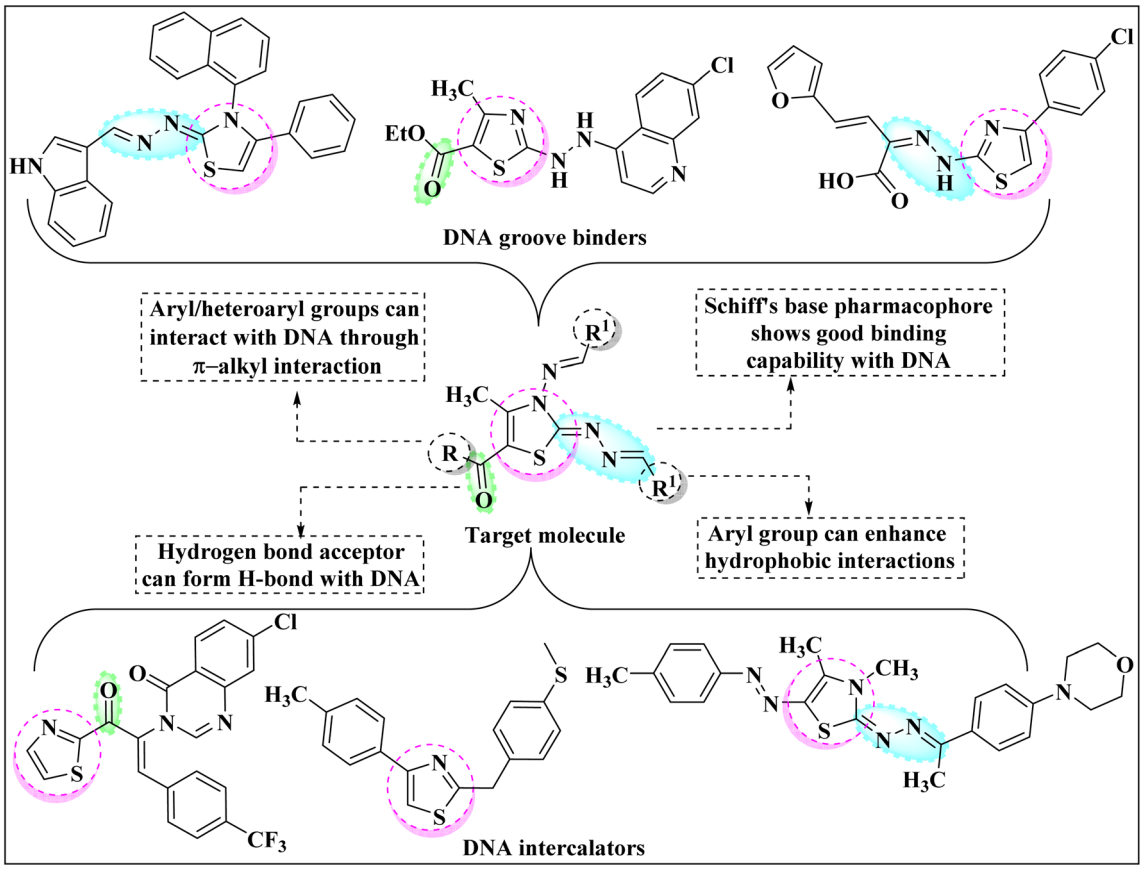

Fig. 1 Potential of thiazole core as DNA binder and rational drug design.

bearing compounds having the capability to interact with DNA.[18–23]

Serum albumins, also known as transporter proteins, are a type of biological receptor that has been extensively studied due to their diverse applications in the binding, transport, and distribution of exogenous and endogenous substances *in vivo*.[24] Serum albumins play a vital role in drug developments as they are the first proteins which comes in contact with the substance after entering the organism. The interaction studies of small molecules with albumin proteins help in the better understanding of pharmacology and pharmacodynamics properties of novel compounds. Bovine Serum Albumins (BSA) exhibit 75%

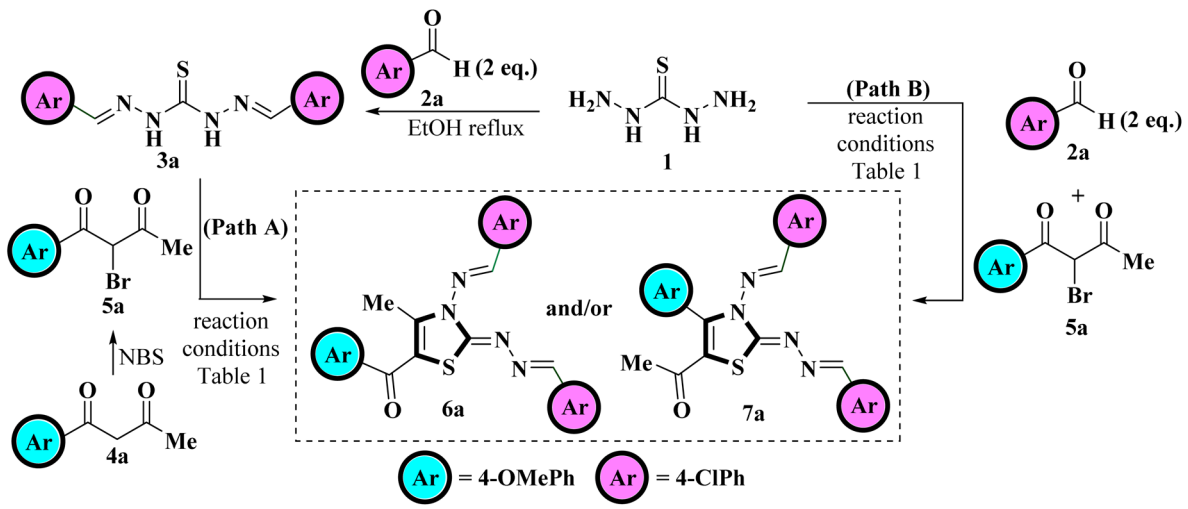

Scheme 1 Model reaction for the synthesis of tetra substituted 2,3-dihydrothiazole.

structural resemblance to Human Serum Albumins, thus widely used as a probe for studying the interactions of small molecules with albumin proteins. The BSA protein mainly consists of three binding sites namely domains I, II and III and each domain is further divided into two subdomains A and B. Recent literature survey reveals that fatty acids prefer to bind to sites IB, IIIA and IIIB whereas small heterocyclic compounds mostly bind to subdomains IIA and IIIA.[25]

Our research group has been enthusiastically indulged in the synthesis of aza-heterocycles using green protocols such as solvent free grinding,[26,27] use of green solvents[28,29] and multicomponent approach.[30,31] Also, our research group has investigated the use of visible light as a sustainable energy source for the synthesis of aza-heterocycles, primarily azoles and exploring the possible biological applications of synthesized compounds as DNA binding agents.[32–36] In light of widespread applications associated with thiazole core and continuing our previous research efforts, it was envisioned to undertake the one-pot multicomponent regioselective synthesis of 5-aroyl-3-((arylidene)amino)-2-((arylidene)hydrazono)-4-methyl-2,3-dihydrothiazole derivatives. The reaction was designed to follow a multicomponent pathway in which thiocarbohydrazide and aldehydes were condensed with α-bromo-1,3-diketones (generated *in situ* by the bromination of unsymmetrical 1,3-diketones with NBS) under visible light in the presence of EtOAc solvent. The final structure of the regioisomer was identified unambiguously using multinuclear 2D NMR techniques *viz.* [^{1}H–^{13}C] HMBC; [^{1}H–^{13}C] HMQC and [^{1}H–^{15}N] HMBC.

Furthermore, the biological potential of the synthesized 2,3-dihydrothiazole derivatives was investigated as DNA and BSA targets using various *in silico* studies including molecular reactivity analysis, Lipinski rule, molecular docking and several spectroscopic techniques *viz.* UV-visible, circular dichroism (CD), steady-state fluorescence and competitive displacement assay.

2. Results and discussion

2.1 Chemistry

Recently Vedula *et al.*, reported the synthesis of coumarin-linked thiazole derivatives *via* one-pot multicomponent reaction of thiocarbohydrazide, aldehydes (2 eq.) and substituted 3-(2-bromoacetate) coumarins in the presence of ethanol as a solvent under microwave irradiation using a catalytic amount of acetic acid.[37]

Taking a lead from here and in continuation of our research work related to the study of the regioselectivity pattern of the reaction of unsymmetrical 1,3-diketones with bi/tri nucleophilic systems herein, we intend to conduct the synthesis of 5-aroyl-3-((arylidene)amino)-2-((arylidene)hydrazono)-4-methyl-2,3-dihydrothiazole. For this purpose, 4-methoxybenzaldehyde **2a** and 1-(4-chlorophenyl)butane-1,3-dione **4a** were chosen as the model substrates to achieve the optimum reaction conditions for the synthesis of the title compounds. The reaction optimization was achieved testing two pathways, **Path A** and **Path B**. Scheme 1 depicts the model reaction for the regioselective synthesis of tetra substituted 2,3-dihydrothiazole following two pathways, **Path A** and **Path B**.

Path A involved the step-wise protocol in which thiocarbohydrazide **1** was first allowed to condensed with 4-methoxy benzaldehyde **2a** under ethanol reflux to generate a hydrazine analogous intermediate **3a**. The reaction was found to be completed within short time spam of 30 minutes as indicated by TLC. The intermediate **3a** was then subjected to react with 2-bromo-1-(4-chlorophenyl)butane-1,3-dione **5a**, generated *in situ* through bromination of 4-chlorophenylbutane-1,3-dione **4a** with mild brominating reagent NBS in polar aprotic (DCM, THF, MeCN, EtOAc) as well as polar protic (EtOH, MeOH, H_2O) solvents under various conditions, including conventional heating and visible light irradiation. A careful monitoring of the reaction progress evidenced that the reaction does not proceed at all in DCM even at elevated temperatures (Table 1, entries 1 and 2) but traces were obtained when the reaction was carried out in THF and MeCN (Table 1, entries 3–5). The reaction was then monitored in EtOAc at elevated temperature and a careful monitoring of the reaction progress through TLC highlights the complete consumption of the reactants within 6 h but furnished the product in low yield (Table 1, entry 6). The reaction was then monitored in polar protic solvents at elevated temperatures but yield of the product was found to be deprived further (Table 1, entries 7–9). To obtain a higher product yield, the reaction was also investigated under visible light irradiation. Astonishingly, the reaction was observed to be completed in a shorter time as indicated by the TLC, where EtOAc was found to provide the desired product with the highest yield (Table 1, entries 10–13). Thus, visible-light-mediated reactions have an advantage over conventional heating because of the short reaction time along with the high product yield.

After examining the reaction conditions for the step-wise protocol (**Path A**), we investigate the course of the reaction using a one-pot multicomponent approach (**Path B**), in which thiocarbohydrazide **1**, 4-methoxybenzaldehyde **2a**, and 2-bromo-1-(4-chlorophenyl)butane-1,3-dione **5a** were allowed to

Table 1 Optimization of reaction conditions

Entry	Solvent	Reaction conditions[a]	Time[b/c]	Yield[d/e/f] (%)
1	DCM	RT	36 h[b/c]	NR[d]
2	DCM	Reflux	6 h[b/c]	NR[d]
3	THF	RT	36 h[b/c]	NR[d]
4	THF	Reflux	6 h[b/c]	Traces[e/f]
5	MeCN	Reflux	6 h[b/c]	Traces[e/f]
6	EtOAc	Reflux	6 h[b]/3 h[c]	42[e]/64[f]
7	MeOH	Reflux	6 h[b]/4 h[c]	35[e]/48[f]
8	EtOH	Reflux	6 h[b]/4 h[c]	38[e]/54[f]
9	H_2O	Reflux	6 h[b]/5 h[c]	30[e]/42[f]
10	MeOH	White LED (9W)	50 min.[b]/40 min.[c]	53[e]/78[f]
11	EtOH	White LED (9W)	45 min.[b]/40 min.[c]	60[e]/83[f]
12	H_2O	White LED (9W)	60 min.[b]/50 min.[c]	40[e]/68[f]
13	EtOAc	White LED (9W)	40 min.[b]/30 min.[c]	72[e]/88[f]

[a] Reaction conditions: reaction of **1** (1 mmol), **2a** (2 mmol) with **4a** (1 mmol) proceeded under a different set of reaction conditions. RT = room temperature. [b] Time taken for step-wise protocol (**Path A**). [c] Time taken for one-pot multicomponent protocol (**Path B**). [d] NR = no reaction. [e] Isolated yield of step-wise reaction (**Path A**). [f] Isolated yield of one-pot multicomponent reaction (**Path B**).

react together in a one-pot. No significant change was observed when the reaction was carried out in DCM, THF and MeCN (Table 1, entries 1–5), whereas considerable enhancement in the product yield was noticed when the reaction was carried out in EtOAc and polar protic solvents (Table 1, entries 6–13) with EtOAc being the most promising solvent when subjected to white LED light yielding 88% product (Table 1, entries 13). Also, reaction was found to be completed in lesser time in one-pot multicomponent strategy than step-wise protocol (Table 1). Thus one-pot multicomponent approach was found to be superior to the step-wise procedure where the reaction proceeds smoothly in polar aprotic EtOAc solvent when irradiated with white LED light and furnished the target product in higher yields.

After getting optimized reaction conditions in hand the next task was to extend the substrate scope of this one-pot multicomponent approach under visible light. To meet the objective, thiocarbohydrazide **1**, was allowed to condense with various aromatic aldehydes **2a–c** and α-bromo-1,3-diketones **5a–f** (generated *in situ* by the bromination of unsymmetrical 1,3-diketones **4a–f** with NBS) under irradiation of white LED light (9W) using EtOAc as a solvent (Scheme 2). This multicomponent approach furnished the target compounds at room temperature in excellent yields in just 30–50 minutes which was later on identified as 5-aroyl-3-((arylidene)amino)-2-((arylidene) hydrazono)-4-methyl-2,3-dihydrothiazole **6a–n** Table 2. The reaction exhibits great functional group tolerance with variously substituted electron-donating as well as electron-withdrawing aldehydes **2a–c** and unsymmetrical 1,3-diketones **4a–f**. It has been noticed that the presence of an electron-donating group at the *para* position of the phenyl ring either on aldehyde or diketone furnished the desired product in high yields in comparison to the electron-withdrawing groups. However, the presence of an electron-donating group at the *meta* position of the phenyl ring or heteroaryl thienyl ring in diketone diminished the product yield.

The IR spectrum of resulted compound **6a** displayed two characteristic absorption bands at 1612 cm^{-1} and 1592 cm^{-1} corresponding to the C=N and carbonyl group respectively. ^{1}H NMR spectrum of the compound **6a** displayed three singlets in the aliphatic region at δ 2.52 ppm, δ 3.88 ppm and δ 3.85 ppm integrated for three protons each corresponding to one set of methyl protons and two sets of methoxy protons along with two more singlets in the aromatic region at δ 10.13 ppm and δ 8.36 ppm integrated for one proton each consistent to two methine protons. Also, a regular pattern of twelve protons in the aromatic region was observed incorporated from one equivalent of 1-(4-chlorophenyl)butane-1,3-dione **4a** and two equivalents of 4-methoxybenzaldehyde **2a** indicating the success of the reaction. Additionally, three sharp singlets in the aliphatic region at δ 55.5 ppm, δ 55.4 ppm and δ 15.6 ppm and one in the aromatic region at δ 187.3 ppm in the ^{13}C NMR spectrum corresponding to one methyl, two methoxy and one carbonyl carbon respectively along with a set of seventeen desired carbon signals in the aromatic region confirms the successful condensation of **1** and **2a** with **4a**.

The IR data, together with ^{1}H and ^{13}C NMR, provide conclusive evidence in favour of the completion of the reaction; however, these techniques alone were insufficient to identify the correct regioisomeric structure of the resulting product. Based on our previous experience with regioselective synthesis of aza-heterocycle, heteronuclear 2D NMR techniques such as [^{1}H–^{13}C] HMBC; [^{1}H–^{13}C] HMQC and [^{1}H–^{15}N] HMBC were utilized to identify the exact regioisomeric structure. The [^{1}H–^{13}C] HMBC spectrum of the resulted compound 5-(4′-chlorobenzoyl)-3-((4″-methoxybenzylidene)amino)-2-(4‴-methoxybenzylidene) hydrazono)- 4-methyl-2,3-dihydrothiazole **6a** exhibits correlation peaks of the methyl protons (δ 2.52 ppm) with C-4 (δ 148.6 ppm) and C-5 (δ 111.3 ppm) indicative of the presence of methyl group at C-4 position of thiazole core. Also, the carbonyl carbon appeared at δ 187.3 ppm displays cross peaks with the 2′/6′- proton (δ 7.74–7.70 ppm) of the phenyl ring signifying the presence of carbonyl carbon next to the phenyl ring. Likewise, [^{1}H–^{15}N] HMBC spectrum demonstrates the cross peaks of the N atom (δ 306.0 ppm) with methyl protons (δ 2.52 ppm) at C-4 position. Furthermore, the diazo N atoms at N-9 (δ 346.5 ppm) and N-10 (δ 278.1 ppm) shows correlation peaks with methylene protons (δ 8.36 ppm) at C-7 position.[28] Lastly, the N atom (δ 278.2 ppm) displays cross peaks with methine protons (δ 10.13 ppm) at C-6 position. These outcomes are in great agreement with our previous results related to the regioselective synthesis of thiazole derivative where carbonyl carbon was found next to the aryl ring and methyl group at C-4 position of the thiazole ring.[26,36] Thus, the structure of regioisomer **6a**

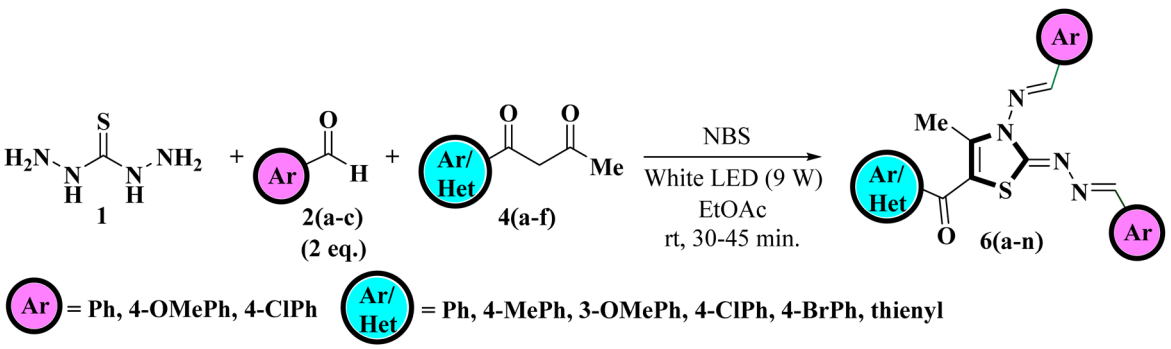

Scheme 2 Visible-light-mediated one-pot multicomponent approach for the regioselective synthesis of title compounds.

Table 2 Substrate scope

Sr, no.	Structure	Compound	Ar/Het	Yield (%)
1	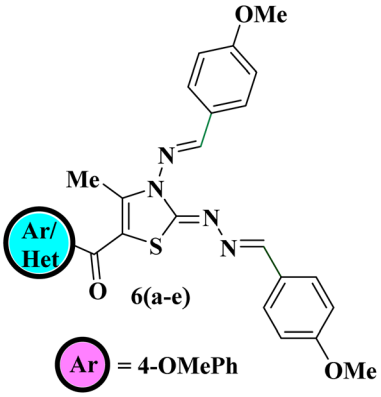	**6a**	4-ClPh	88
2		**6b**	4-BrPh	90
3		**6c**	Ph	92
4		**6d**	4-MePh	93
5		**6e**	Thienyl	85
6	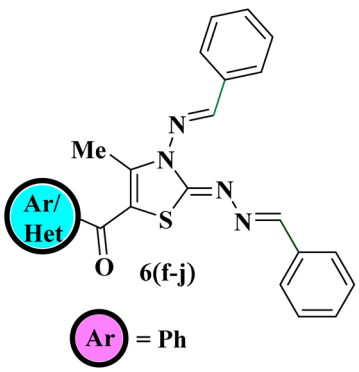	**6f**	4-BrPh	87
7		**6g**	Ph	89
8		**6h**	4-MePh	92
9		**6i**	3-OMePh	84
10		**6j**	Thienyl	85
11	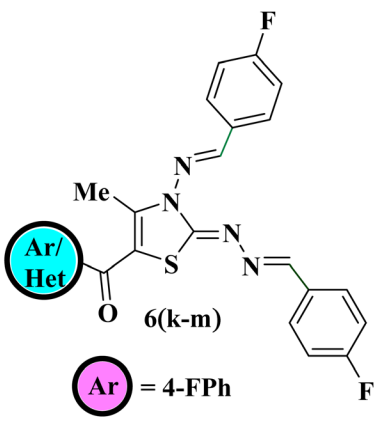	**6k**	4-BrPh	88
12		**6l**	4-MePh	87
13		**6m**	3-OMePh	83
14		**6n**	Thienyl	82

was confirmed as 5-(4′-chlorobenzoyl)-3-((4″-methoxybenzylidene)amino)-2-(4‴-methoxybenzylidene)hydrazon-o)-4-methyl-2,3-dihydrothiazole. A similar correlation pattern of [^{1}H–^{13}C] HMBC; [^{1}H–^{13}C] HMQC and [^{1}H–^{15}N] HMBC were noticed for 5-(4′-bromobenzoyl)-3-((4″-methoxybenzylidene) amino)-2-(4‴-methoxybenzylidene)hydrazono)-4-methyl-2,3-dihydrothiazole **6b** as shown in Fig. 2.

The plausible mechanistic pathway for the regioselective synthesis of title 5-aroyl-3-((arylidene)amino)-2-((arylidene) hydrazono)-4-methyl-2,3-dihydrothiazole derivatives is illustrated in Scheme 3. Primarily, *in situ* formation of hydrazine analogous intermediate **3** was taken place by the reaction of variously substituted aldehydes **2** and thiocarbohydrazide **1**. The homolytic bond fission of C–Br bond of α-bromo-1,3-diketones **5** and S–H bond of hydrazine analogous **3** results in the formation of two free radical intermediates **8** and **9** respectively due to the exposure of visible light.[38] These two free radicals were then combined *via* electron sharing to form S-alkylated intermediate **10**. Following that, the nucleophilic attack of a lone pair of electrons over the N atom take place on

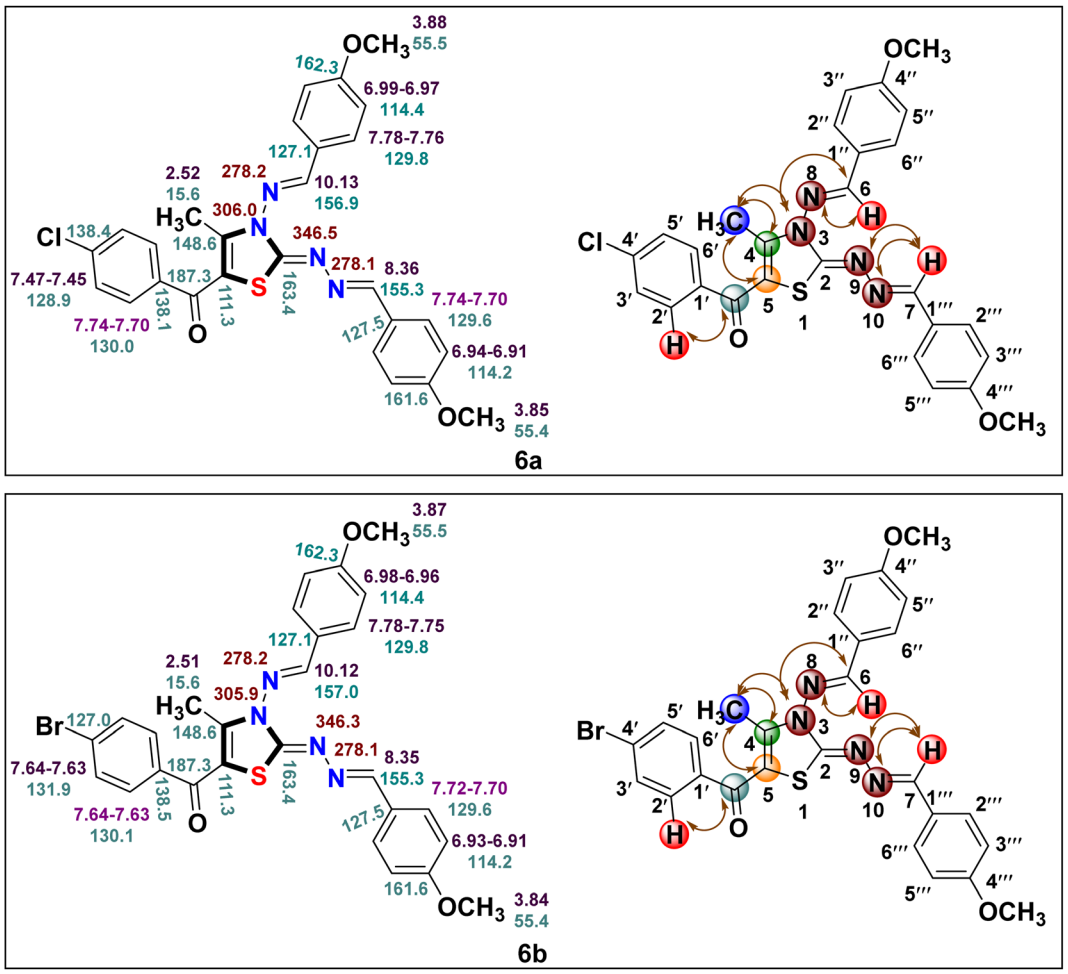

Fig. 2 ^{1}H (in purple), ^{13}C (in blue) and ^{15}N (in brown) chemical shifts for compounds **6a** and **6b** along with correlation representation.

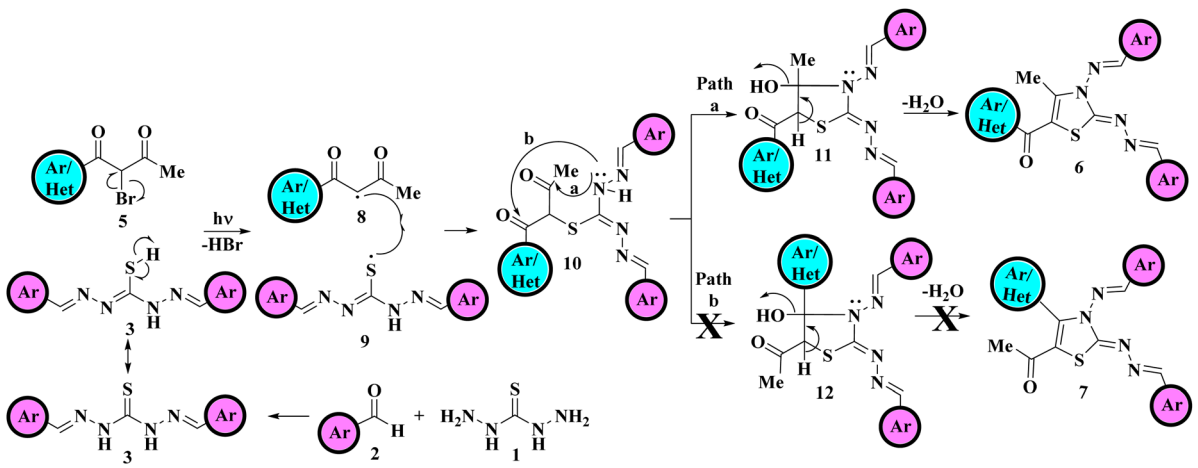

Scheme 3 Mechanistic pathway for the one-pot multicomponent approach towards regioselective synthesis of 2,3-dihydrothiazole derivatives **6**.

the carbonyl carbon. As two electrophilic carbonyl centres of different electrophilicities are present thus two paths are possible **Path a** and **Path b.** However, attack take place at the less sterically hindered carbonyl carbon next to the methyl group yields the cyclized intermediate **11**, this ruled out the possibility of formation of other regioisomer **12.** Finally,

cyclised regioisomer **11** underwent removal of water to furnished the final 2,3-dihydrothiazole derivatives **6**.

2.2 Biological assay

2.2.1 Molecular reactivity analyses. It is a well-known fact that the stability of a molecule is an important parameter to identify its reactivity which in turn depends upon the energies of frontier orbitals.[39] Frontier orbitals are mainly classified into two categories: highest occupied molecular orbitals (HOMO) and lowest unoccupied molecular orbitals (LUMO). The energies of the frontier orbitals of all synthesised compounds are shown in the Table 3 and were determined through a theoretical study using mm + force field energy minimization (PerkinElmer Chem3D 15.0.0.106). Higher the gap between frontier orbitals, more is the stability of the compound and *vice versa*. The energy gap between the frontier orbitals ($\Delta E = E_{LUMO} - E_{HOMO}$) for all the synthesized 2,3-dihydrothiazole derivatives **6a–n** are displayed in the Table 3 which clearly indicates the highest stability of **6c** derivative and lowest stability of **6n** derivative (Fig. 3). As, HOMO is mainly an electron donor whereas, LUMO depicts the acceptance ability, thus energies of frontier orbitals also help to determine the ionization potential (IP) and electron affinity (EA) of the compound which was evaluated on the basis of Koopman theorem according to which: IP $= -E_{HOMO}$ and EA $= -E_{LUMO}$. Thus, compound **6g** has the highest IP, indicating a high energy requirement for the removal of an electron from

Table 3 Frontier orbitals energy and global reactivity descriptors of compound 4a–g

Comd.	E_{HOMO}	E_{LUMO}	ΔE	IP	EA	η	S	χ	μ	ω
6a	−3.569	−2.283	1.286	3.569	2.283	0.643	0.777	2.926	−2.926	6.657
6b	−3.692	−2.285	1.407	3.692	2.285	0.703	0.710	2.988	−2.988	6.347
6c	−4.190	−2.290	1.900	4.190	2.290	0.950	0.526	3.240	−3.240	5.525
6d	−3.994	−2.289	1.705	3.994	2.289	0.852	0.586	3.141	−3.141	5.788
6e	−2.626	−2.269	0.357	2.626	2.269	0.178	2.801	2.447	−2.447	16.780
6f	−3.783	−2.284	1.499	3.783	2.284	0.749	0.667	3.033	−3.033	6.139
6g	−4.322	−2.952	1.370	4.322	2.952	0.685	0.729	3.637	−3.637	9.655
6h	−4.063	−2.287	1.776	4.063	2.287	0.888	0.563	3.175	−3.175	5.676
6i	−4.178	−2.298	1.880	4.178	2.298	0.940	0.531	3.238	−3.238	5.577
6j	−2.992	−2.282	0.710	2.992	2.282	0.355	1.408	2.637	−2.637	9.794
6k	−3.676	−2.282	1.394	3.676	2.282	0.697	0.717	2.979	−2.979	6.366
6l	−3.978	−2.285	1.693	3.978	2.285	0.846	0.590	3.131	−3.131	5.792
6m	−4.100	−2.286	1.814	4.100	2.286	0.907	0.551	3.193	−3.193	5.620
6n	−2.535	−2.256	0.281	2.537	2.256	0.140	3.558	2.396	−2.396	20.438

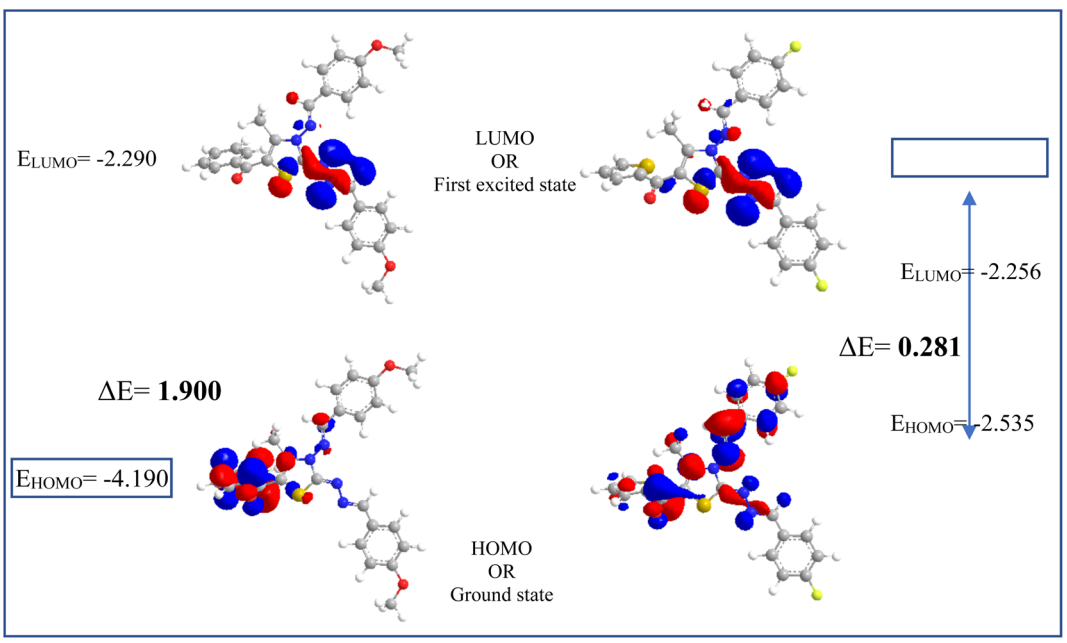

Fig. 3 Frontier orbitals and energy gap between them for the compounds **6c** and **6n**.

the HOMO, whereas compound **6n** has the lowest EA, signifying the ease of the compound undergoing electrophilic reaction.

Furthermore, Pearson and Parr describe some descriptors *viz.*, chemical hardness ($\eta = \frac{(IP - EA)}{2}$), chemical softness ($S = \frac{1}{2\eta}$), electronegativity ($\chi = \frac{(IP + EA)}{2}$), chemical potential ($\mu = \frac{-(IP + EA)}{2}$) and electrophilicity index ($\omega = \frac{\mu^2}{2\eta}$) known as Global reactivity descriptors[40] and are highlighted in the Table 3.

From Table 3 it was concluded that compound **6c** has highest value of hardness ($\eta = 0.950$ eV) thus be the most stable and inert among all the tested compounds whereas, **6n** was found to exhibits the highest value of softness ($S = 3.558$ eV) indicates the lesser stability and more reactivity of the ligand. Furthermore, the electronegativity was found to be highest for the compound **6g** ($\chi = 3.637$ eV), indicates the high reducing potential of the ligand **6g**. The electrophilicity index, ability of a ligand to accept an electron, was found to largest for the compound **6n** ($\omega = 20.438$ eV).

2.2.2 Lipinski's rule of five. Recently, Computational techniques have emerged as an important tool in identifying whether a new compound be a promising drug or not, thereby reducing the number of experimental drug trials and helps in the drug development. Thus, the ADMET (absorption, distribution, metabolism, excretion, and toxicity) properties of ligands, also known as pharmacokinetic properties, aid in determining their action within the human body. In this regard to recognize the drug candidature of the synthesized 2,3-dihydrothiazole derivatives their pharmacokinetic properties were evaluated using an online tool SwissADME (**https://www.swissadme.ch**). The Lipinski rule of 5 provides the grounds to determine the drug-likeness of newly synthesized ligands entities. According to the rule, ligands with more than 10 hydrogen bond acceptors, 5 hydrogen bond donors, 10 rotatable bonds, CLogP greater than 5, total topological polar surface area (TPSA) more than 140 A°, and molecular weight above 500 Da exhibits poor absorption or permeability.[41] As a result, ligand entities that fall outside of these ranges have poor drug bioavailability. The results of Lipinski rule of 5 are highlighted in Table 4. All the synthesized 2,3-dihydrothiazole derivatives have number of hydrogen bond donors, number of hydrogen bond acceptors and number of rotatable bonds within the prescribed range. The TPSA of all the synthesized compounds is within the specific range which is an indicator of absorption of a ligand in intestine. Also, the molecular weights of most of the derivatives lie inside the range of 500 Da with few exceptions (**6a**, **6b**, **6f** and **6k**). The molecular weight of a ligand is an important parameter in determining drug bioavailability; however, this does not rule out the possibility of a drug being bioavailable if molecular weight exceeds 500 Da. Furthermore, CLog *P* (logarithm of partition coefficient between water and *n*-octanol) helps to determine the compound hydrophilicity and ligands with CLog $P < 5$ were found to exhibit good oral-bioavailability but unfortunately all the synthesized derivatives have slightly higher value of CLog *P*. Also, all the synthesized derivatives have a Log *S* value over −3.0, indicates the poor solubility of the compounds in water. Furthermore, Log K_p values, a parameter used to describe the skin permeability are within the standard range of −1.0 to −8.0. Thus, majority of the synthesized compounds have the values of Lipinski rule of 5 within the desired range with few derivatives showing one or two violations. However, compounds with two or more violations (**6k**, **6l** and **6m**) of the Lipinski rule are found to have poor bioavailability.[42]

2.2.3 Molecular docking analysis: DNA. The use of molecular docking studies has increased in past decade as a result of their widespread applications in rational drug design and the discovery of novel drugs. Molecular docking analysis helps in the recognition of favourable conformations between drugs and biomacromolecules such as nucleic acids and proteins with the lowest overall free energy.[43] Also, small organic molecules preferred to bind in the minor grove of the DNA due to the narrow shape of the minor grove and electrostatic factors.

For the docking analysis of the synthesized compounds with ct-DNA, structure of the DNA was required which was obtained from the protein data bank (PDB ID:1bna) having a sequence [d $(CGCGAATTCGCG)_2$]. The binding affinities of all the synthesized derivatives with ct-DNA along with their three-

Table 4 Lipinski rule of five

C. No.	TPSA	MW	cLogP	nHBA	nHBD	RB	Violations	Log *S*	Log K_p
6a	105.8	519.02	5.8	6	0	8	1	−7.1	−4.9
6b	105.8	563.47	5.8	6	0	8	1	−7.4	−5.1
6c	105.8	484.58	5.2	6	0	8	0	−6.5	−5.1
6d	105.8	498.61	5.5	6	0	8	0	−6.8	−5.0
6e	134.0	490.61	5.2	6	0	8	0	−6.5	−5.1
6f	87.3	503.42	5.2	4	0	6	0	−6.5	−5.1
6g	87.3	424.53	5.2	4	0	6	0	−6.5	−5.1
6h	87.3	438.55	5.2	4	0	6	0	−6.5	−5.1
6i	96.5	454.55	5.2	5	0	7	0	−6.5	−5.1
6j	115.6	430.55	5.2	4	0	6	0	−6.5	−5.1
6k	87.3	539.40	6.4	6	0	6	2	−7.6	−4.8
6l	87.3	474.53	6.4	6	0	6	2	−6.7	−4.8
6m	96.5	490.53	5.8	7	0	7	2	−6.7	−4.8
6n	115.6	466.54	5.8	6	0	6	1	−6.7	−4.8

Table 5 3D poses of the most stable DNA-ligand interaction, binding affinity and interaction sites

Cmpd.	3D plot of binding interactions	Binding affinity (kcal mol^{-1})	H-bond	Residual nitrogenous base interactions: Hydrophobic/pi–cation/ pi–anion/pi–alkyl interactions	Residual nitrogenous base interactions: van der Walls interactions
6a	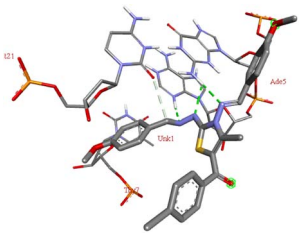	−8.4	DG A:4, DA A:5	DT A:7, DC B:21	—
6b	No interactions found	−7.0	—	—	—
6c	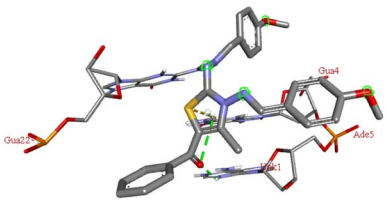	−7.3	DG A:4, DA A:5, DG B:22	—	—
6d	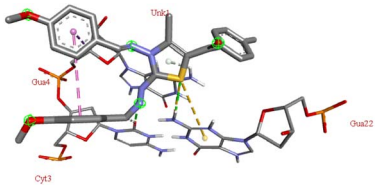	−6.7	DC A:3, DG B:22	DG A:4	—
6e	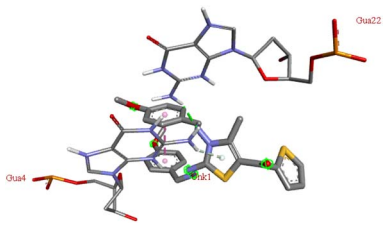	−6.1	DG B:22	DG A:4	—
6f	No interactions found	−6.8	—	—	—
6g	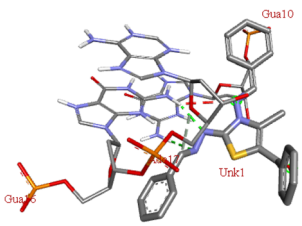	−7.8	DG A: 10, DG B:16	DA B:17	—
6h	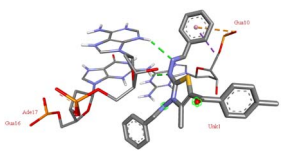	−8.1	DG B: 16, DA B:17	DG A:10	—
6i	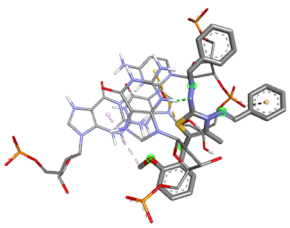	−7.6	DG B: 16	DC A:11, DG A:12	—

Table 5 (*Contd.*)

Cmpd.	3D plot of binding interactions	Binding affinity (kcal mol^{-1})	Residual nitrogenous base interactions		
			H-bond	Hydrophobic/pi–cation/ pi–anion/pi–alkyl interactions	van der Walls interactions
6j	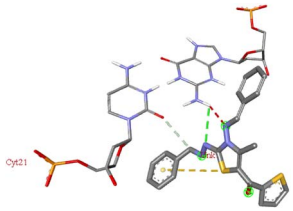	−6.0	DG A: 4	DC B:21	—
6k	No interactions found	−5.8			—
6l	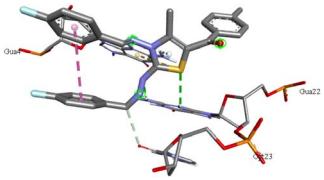	−7.8	DG B:22	DG A:4, DC B:23	—
6m	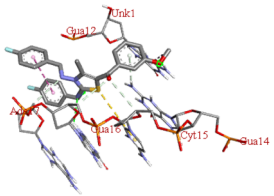	−7.8	DG B: 16	DG A:12, DG B:14, DC B:15, DA B:17	—
6n	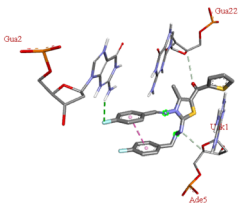	−6.6	DG A:2	DA A:5, DG B:22	—

dimensional poses and interactive binding sites are displayed in Table 5. All the derivatives were found to bind with DNA in the minor groove through non-covalent interactions including H-bond, pi-anion, pi–pi stacking and pi-donor. From the outcomes it has been witnessed that bromo derivatives (**6b**, **6f** and **6k**) were fail to interact with ct-DNA due to large size of bromine atom whereas, thienyl derivatives (**6e**, **6j** and **6n**) were found to have low binding affinities for ct-DNA. Furthermore, compound **6a** was found to exhibit maximum binding affinity for the ct-DNA molecule.

The compound 5-(4′-chlorobenzoyl)-3-((4″-methoxybenzylidene)amino)-2-(4‴-methoxybenzylidene) hydrazono)-4-methyl-2,3-dihydrothiazole **6a** was found to exhibit maximum binding affinity −8.4 kcal mol^{-1} for the ct-DNA molecule. Furthermore, the N atoms of the hydrazinyl residue and imino group of the compound **6a** were found to participate in H-bonding with guanidine and adenine residues present at 4th and 5th position of the DNA sequence respectively. Fig. 4 displays the lowest energy 2d and 3d poses of the interaction between ligand **6a** and DNA.

Although, compound **6a** shows one violation of Lipinski rule due to its molecular weight exceeding 500 Da, but high binding affinity with DNA and lesser stability/high reactivity ($\Delta E = 1.286$ eV) of **6a** after thienyl derivatives make it a good candidate for further binding studies with DNA using various spectroscopic techniques such as UV-absorption, fluorescence, and CD spectroscopy.

2.2.4 UV-visible spectroscopy. The use of UV-visible spectroscopy has increased in the past decade due to its various applications, including the early identification of interactions between ligands and biomacromolecules. Also, UV-visible spectroscopy is helpful in understanding the binding mode of ligands with DNA (interactor or grove binder). An absorption maxima for native DNA at 260 nm owing to $\pi \rightarrow \pi^*$ transitions is highly significant in discovering ligand-DNA interactions since any change in the microenvironment of the DNA in the presence of a ligand affects this maximum.[15] In literature, it is documented that a bathochromic or hypochromic shift has been observed if a ligand intercalates with DNA helix whereas, in the case of grove binding mode hyperchromic or hypsochromic shift in the absorption maxima has been found.

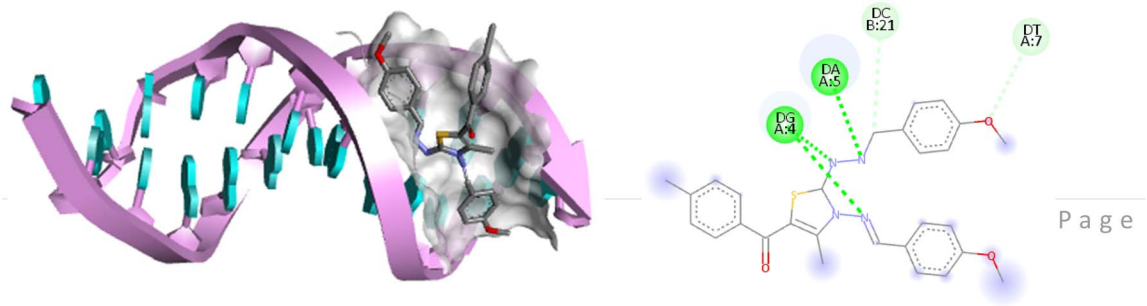

Fig. 4 2D and 3D poses of the interaction of ligand **6a** with DNA protein.

Thus, UV-visible analysis was carried out to identify the interactions between test ligand **6a** and ct-DNA. In the process, UV-visible spectra of a fixed concentration of DNA in Tris–HCl (67 μM, pH 7.2) were examined in the absence as well as the presence of increasing concentration of ligand **6a** (0–20 μM) in the spectral range of 200–500 nm at room temperature. An absorption maximum at 260 nm was observed for the native DNA which shows an increment with an increasing concentration of ligand **6a**. From the Fig. 5, it is evident that a hyperchromic shift in the absorption maxima occurs with increasing concentration of ligand **6a** suggesting the groove binding mode ligand.

2.2.5 Fluorescence quenching analysis. Fluorescence quenching analysis is a simple, effective and significant technique to identify the binding characteristics of the fluorophore (biomacromolecule) and quencher (ligand). For the process, the emission spectra of ct-DNA in Tris–HCl (67 μM, pH 7.2) were recorded in the spectral range of 290–500 nm in the absence and presence of increasing concentrations of ligand **6a** (0–24 μM), with the excitation wavelength (λ_{ex}) fixed at 290 nm. An emission maximum at 325 nm was observed for native DNA which underwent a continuous decrease with a gradual increment in the ligand concentration and finally quenching of the emission spectra at a high concentration of ligand confirms the binding of the ligand with DNA. An identical experiment was conducted at three different temperatures: 298, 303, and 308 K (Fig. 6) yielding similar outcome. According to reports, a decrease in emission intensity with increasing ligand concentration is indicative of the grove binding mode of ligand, whereas an increase in emission intensity was often observed in the case of intercalation binding of ligand into base pairs of DNA.

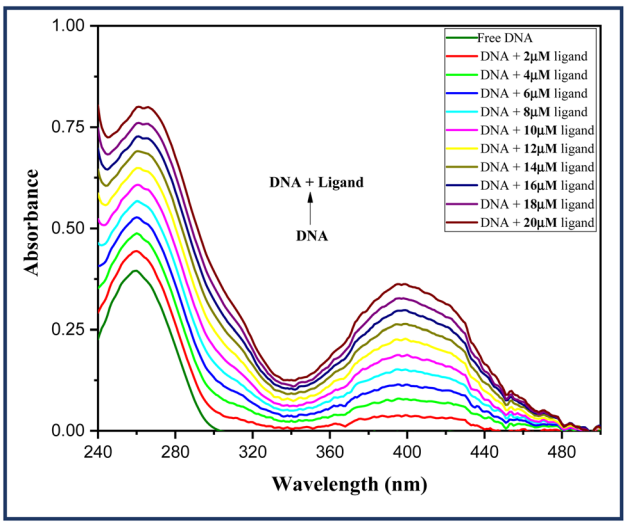

Fig. 5 Absorption spectra of DNA (67 μM) in the absence and presence of an increasing concentration of ligand **6a** (0–20 μM).

Several molecular mechanisms are responsible for the quenching of the emission intensity of DNA with increasing ligand concentration but mainly depend upon two mechanisms namely static quenching and dynamic quenching. Static quenching is referred as a ground state phenomenon in which a complex is formed between fluorophore and quencher whereas, dynamic quenching is an excited state phenomenon that arises due to the collision or diffusion between fluorophore and quencher.[44] The extent of quenching is determined in terms of a constant known as the Stern–Volmer constant using eqn (1).

$$\frac{F_o}{F} = 1 + K_{sv}[Q] = 1 + K_q\tau_o[Q] \quad (1)$$

where F_o and F refers to the fluorescence intensity of fluorophore in the absence and presence of an increasing concentration of ligand respectively. K_q and K_{sv} are the quenching constant ($K_{sv} = K_q\ \tau_o$) and Stern–Volmer constant respectively, τ_o (10^{-8} in case of biomolecules) is the average fluorescence lifetime of the biomolecule in the absence of quencher and $[Q]$ defines the molar concentration of quencher.

In order to determine the mechanism of quenching followed during the interaction between DNA and ligand **6a**, Stern–Volmer plots were utilized at three different temperatures: 298, 303 and 308 K by using the fluorescence intensity at 325 nm (Fig. 7a). A straight-line graph was plotted between the ratio of fluorescence intensity at 325 nm in the absence (F_o) and presence (F) of ligand **6a** against the increasing molar concentration $[Q]$ of ligand **6a** by keeping the intercept constant at 1. The slope of the plot provides the values of the Stern–Volmer constant K_{sv} and the quenching constant K_q Table 6. It has been observed that in the case of dynamic mechanism, the quenching constants show an increment with the rise in temperature as

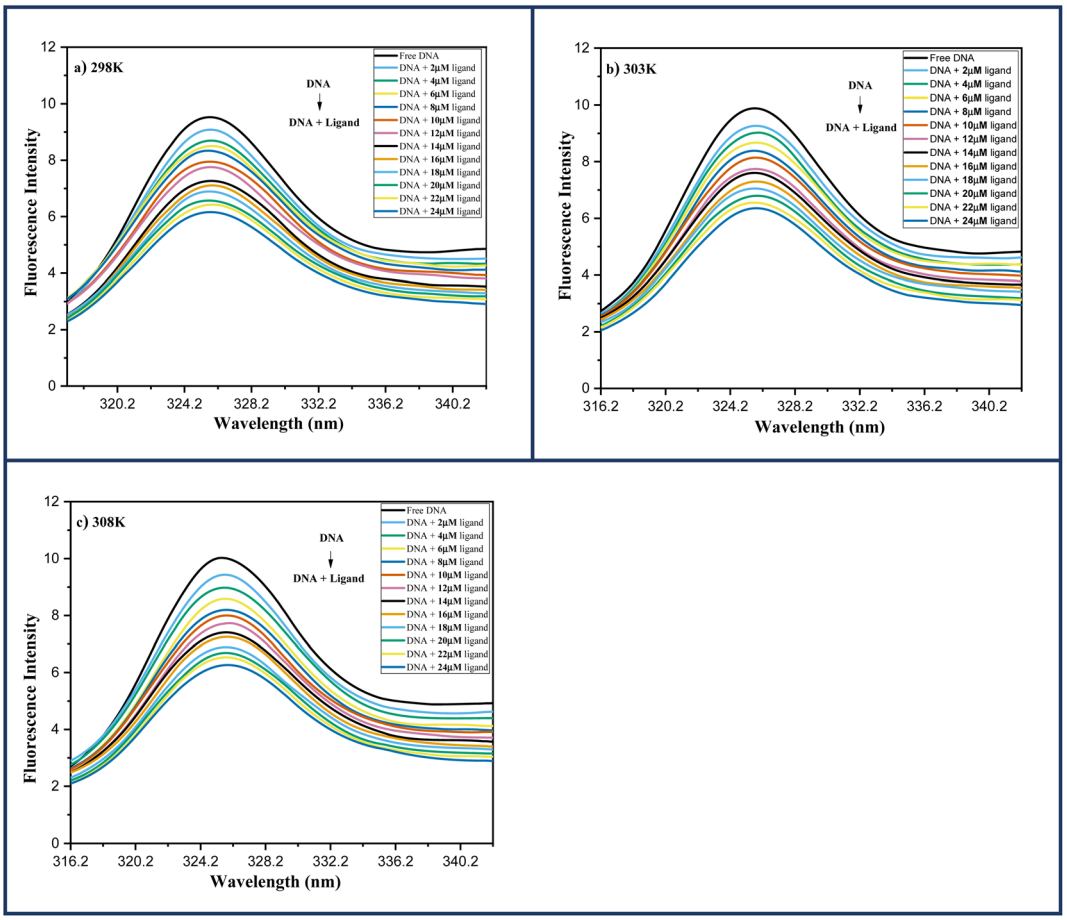

Fig. 6 Fluorescence spectra of DNA-**6a** (67 μM) complex system with increasing ligand concentration **6a** (0–24 μM) at (a) 298 K; (b) 303 K; (c) 308 K.

high-temperature favours faster diffusion and results in more collisions between fluorophore and quencher whereas, in the case of static mechanism the quenching constants decrease with a rise in temperature as the complex of fluorophore and quencher dissociates at higher temperature. From Table 6, it is evident that the quenching constants K_{sv} and K_q goes on decreasing with an increase in temperature suggesting the static mechanism to be followed during the interaction between DNA and ligand **6a**.

2.2.5.1 Identification of binding constant and number of binding sites. How effectively a quencher can interact with fluorophore can be identified in terms of binding constant (K_b) using double-logarithmic Scatchard's eqn (2).[45] Furthermore, the same equation can also be used to calculate the number of binding sites n.

$$\mathrm{Log}\frac{(F_o - F)}{F} = \mathrm{Log}\ K_b + n\mathrm{Log}[Q] \quad (2)$$

where parameters F_o and F define the fluorescence intensity of fluorophore in the presence and absence of quencher **6a**. $[Q]$, n and K_b are the molar concentration of ligand **6a**, number of binding sites and binding constant respectively.

A linear regression was obtained when the logarithmic ratio of the difference in fluorescence intensity of fluorophore in the absence and presence of quencher **6a** to the fluorescence intensity of fluorophore in the presence of quencher **6a** was plotted against the molar concentration of the quencher **6a** (Fig. 7b). The slope and intercept of this linear regression help to determine the number of binding sites n and binding constants K_b respectively at three different temperatures: 298, 303 and 308 K and are presented in the Table 6. The value of binding constant K_b at all three temperatures is of the order 10^4 which is in great agreement with the literature value indicating the grove binding mode of ligand **6a** with DNA.[46] Furthermore, the number of binding sites nearly 1 at all three temperatures indicates 1 : 1 binding stoichiometry of the ligand **6a** with DNA which also indicates only one mode of binding *i.e.*, grove binding.

Also, limit of detection (LOD) was calculated for each titration and the results are highlighted in Table S1.†

2.2.5.2 Identification of binding forces. When a drug interacts with a biomacromolecule, certain types of forces exhibit between them namely hydrophobic force, hydrogen bond, van der Waals interaction or electrostatic interaction.[47] The sign of thermodynamic parameters, specifically change in enthalpy ($\Delta H°$) and change in entropy ($\Delta S°$) provide access to identify these forces. The following three scenarios have been found to

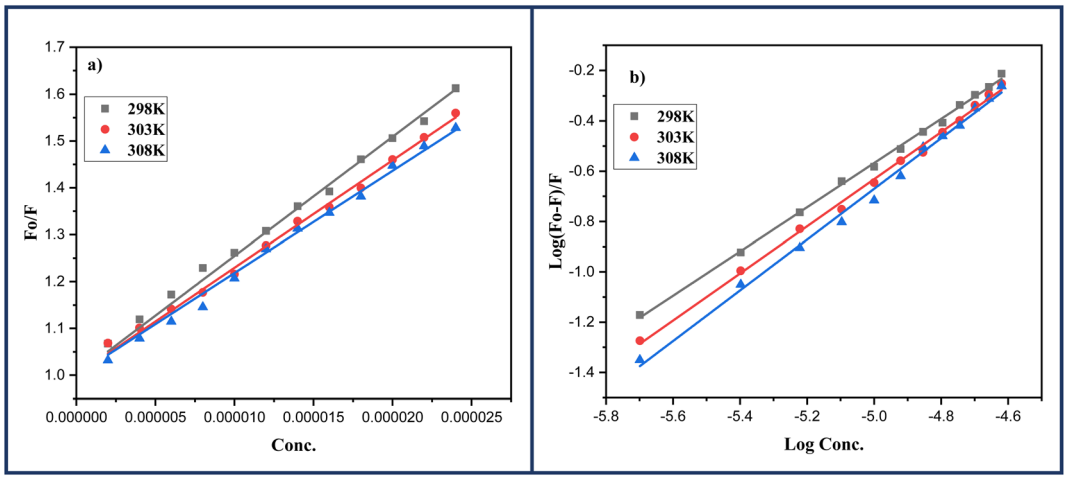

Fig. 7 (a) Stern–Volmer; (b) Scatchard's plots for the DNA-6a complex systems at varying three different temperatures: 298, 303 and 308 K respectively.

Table 6 Stern–Volmer constant (K_{sv}), quenching constant (K_q), binding constant (K_b), number of binding sites (n), Gibbs free energy ($\Delta G°$) and thermodynamic parameters ($\Delta H°$ & $\Delta S°$)

T (K)	$K_{sv} \times 10^4$ (M^{-1})	$K_q \times 10^{12}$ (M^{-1} s^{-1})	Log K_b	$K_b \times 10^4$ (M^{-1})	n	$\Delta G°$ (kJ mol^{-1})	$\Delta H°$ (kJ mol^{-1})	$\Delta S°$ (J mol^{-1} K^{-1})
298	(2.54 ± 0.02)	(2.54 ± 0.02)	4.37 ± 0.11	2.34	1.00 ± 0.02	−24.9	−94.9	−235.05
303	(2.29 ± 0.02)	(2.29 ± 0.02)	4.05 ± 0.08	1.12	0.93 ± 0.01	−23.5		
308	(2.18 ± 0.02)	(2.18 ± 0.02)	3.82 ± 0.05	0.66	0.87 ± 0.01	−22.5		

aid in predicting the binding forces displayed by ligands and biomacromolecules during the interaction process.

(i) $\Delta H° > 0$ & $\Delta S° > 0$ shows hydrophobic interactions

(ii) $\Delta H° < 0$ & $\Delta S° > 0$ represents electrostatic interactions

(iii) $\Delta H° < 0$ & $\Delta S° < 0$ demonstrates van der Waals interaction or hydrogen bonding.

For this purpose, van't Hoff eqn (3) was utilized in order to determine the values of $\Delta H°$ & $\Delta S°$.

$$\Delta G^{\circ} = -2.303RT \log K_b = \Delta H^{\circ} - T\Delta S^{\circ} \quad (3)$$

The slope and the intercept of linear regression obtained by the plot of the logarithm of binding constant K_b and reciprocal of temperature ($1/T$) provide the value of $\Delta H°$ & $\Delta S°$ respectively (ESI Fig. S1†). The negative values of both the thermodynamic parameters ($\Delta H° = -94.9$ kJ mol^{-1} & $\Delta S° = -235.05$ J mol^{-1} K^{-1}), indicating that hydrogen bonding or van der Waals interaction has occurred between ligand 6a and DNA during the interaction process Table 6.

Apart from this, the spontaneity of the binding process at all three studied temperatures: 298, 303 and 308 K was also determined in the terms of the change in Gibbs free energy ($\Delta G°$). The negative values of the $\Delta G°$ at all three temperatures indicate the spontaneity of the binding process Table 6. ESI Fig. S1† depicts the graphical representation of thermodynamic parameters $\Delta H°$, $\Delta S°$ and $\Delta G°$.

2.2.6 Displacement assay. Although, UV-visible studies and fluorescence analysis provide indications in the favour of the grove binding mode of the interaction of ligand **6a** with ct-DNA but do not provide any strong conclusive evidence. It has been noticed that when a drug competitively substitutes a dye from the DNA duplex, it is expected to interact with DNA in the same way that bound dye does. Thus, displacement assay was carried out using two fluorogenic dyes whose binding modes were already well established namely ethidium bromide (EtBr) and Hoechst-33258 (Ho), to confirm the binding mode of ligand **6a** with DNA. The former is known to intercalate between base pairs of DNA whereas the latter is a well-known grove binding agent.[48]

In this experiment, the emission spectra of DNA-Ho (70 : 1) and DNA-EtBr (10 : 1) complexes in Tris–HCl (pH 7.2) were recorded in the absence and presence of increasing concentrations of ligand **6a** (0–35 μM). Both the spectra were recorded at room temperature in the spectral range of 360–600 nm for the DNA-Ho complex and 500–700 nm for DNA-EtBr by keeping the excitation wavelength fixed at 343 nm and 475 nm respectively. Fig. 8 clearly shows that the emission spectra of the DNA-EtBr complex do not alter as the concentration of ligand **6a** increases, ruling out the possibility of ligand **6a** acting as an intercalator. Furthermore, the DNA-HO complex emission spectra show a gradual decrease with increasing ligand concentration **6a**, confirming the grove binding mode of ligand **6a** with DNA.

2.2.7 Circular dichroism. According to reports, the majority of naturally occurring biomacromolecules exhibit intrinsic

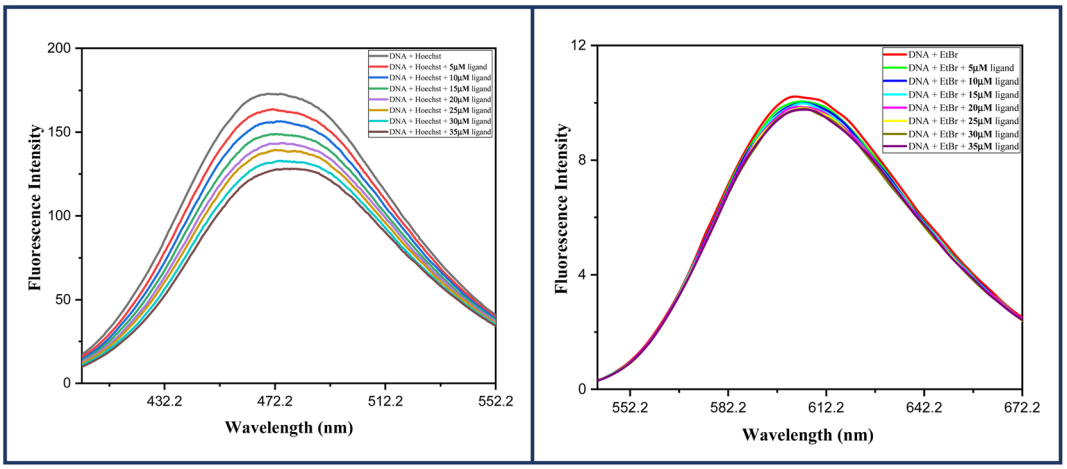

Fig. 8 DNA-Hoechst and DNA-EtBr complexes competitive displacement plots in the absence and in the presence of an increasing concentration **6a** (0–35 μM) in DMSO at pH = 7.2.

circular dichroism in the ultraviolet range, which aids in the identification of interactions between biomacromolecules and ligands and in the case of DNA it is also helpful in the prediction of binding mode as well. Thus, with this viewpoint, the CD spectroscopy technique was employed to recognize any structural changes in the secondary structure of DNA in the presence of ligand **6a**. It has been noticed that the secondary structure of DNA shows alternation when a ligand inserts into the base pairs (intercalation mode of binding) whereas the secondary structure of DNA remains unaltered when interacting through grove binding mode. Also, the CD spectrum of B-form of double-stranded ct-DNA exhibits two characteristic peaks one in the negative region appears nearly at 245 nm and the other in the positive region appears around 275 nm corresponding to the helicity of the right-handed double-stranded DNA and π–π base stacking interactions respectively.[49]

For this purpose, the CD spectrum of pure DNA in Tris–HCl (67 μM, pH 7.2) was recorded in the absence as well as in the presence of an increasing concentration of ligand **6a** (0.2–1.0 μM) in the spectral range of 220–300 nm. There has been no evident change in either the negative or positive peak (ESI Fig. S2†). Thus, CD spectroscopy provides conclusive evidence in favour of grove binding mode of ligand **6a** with DNA and ruled out the possibility of intercalation binding.

2.2.8 Molecular docking analysis: BSA. The crystallographic structure of the BSA protein was downloaded from the protein data bank (PDB ID: 4F5S). All the synthesized derivatives were allowed to docked with the BSA protein and their binding affinities along with their three-dimensional poses and interactive binding sites are displayed in Table 7.

From the values of binding affinity, we can say that the synthesized compounds bind more effectively with protein than DNA. However, the outcomes of the protein binding are almost similar to that of DNA binding where bromo derivatives (**6b**, **6f** and **6k**) again fail to interact with BSA protein. Also, thienyl derivatives (**6e**, **6j** and **6n**) were found to have low binding affinities for protein similar to ct-DNA. Furthermore, almost all the derivatives bind with the protein through non-covalent interaction with B chain of the protein with few exceptions where derivatives **6c** and **6h** were found to interact with protein through chain A.

Among all the tested derivatives 5-(4′-chlorobenzoyl)-3-((4″-methoxybenzylidene)amino)-2-(4‴-methoxybenzylidene) hydrazono)-4-methyl-2,3-dihydrothiazole **6a** was observed to exhibits the highest binding affinity −9.6 kcal mol^{-1}. Ligand **6a** binds with BSA protein through H-bonding with LYS B:116 and also possesses other non-covalent interactions such as hydrophobic, pi-cation, pi-anion, pi–alkyl interactions with other amino acid residues *viz.*, LYS B:132, LYS B:136, TYR B:137, PRO B:117, MET B:184, TYR B:160, ILE B:181, ARG B:185, LEU B:115, PRO B:113, GLU B:140, GLU B:125. Fig. 9 displays the lowest energy 2d and 3d poses of the interaction between ligand **6a** and BSA protein.

Through molecular docking the binding interactions of the ligands not only with BSA but also with other biologically relevant proteins like trypsin and glutathione were investigated. The most suitable thiazole derivative **6a** was docked with trypsin (PDB ID: 2zq1) and glutathione (PDB ID: 3dk9). The outcomes reveals that the binding affinity of the thiazole derivatives for trypsin and glutathione are −6.3 and −8.9 kcal mol^{-1} respectively. The 2D poses of the interaction of ligand 6a with trypsin and glutathione are presented in Fig. S3† given below.

The affinity of the synthesized thiazole derivatives for BSA is highest, indicating a strong interaction and supporting its role as a BSA targeting agent but the values for trypsin and glutathione also suggest potential interactions with these proteins as well. Thus, in conclusion it has been proposed that the synthesized thiazole derivatives are not specific for BSA protein only but can also interact with other proteins as well specifically trypsin and glutathione.

Again, compound **6a** was selected for further *in vitro* analysis with BSA protein using various spectroscopic techniques due to high binding affinity and lesser stability/high reactivity.

Table 7 3D poses of the most stable BSA-ligand interaction, binding affinity and interaction sites

Cmpd	3D plot	Binding affinity (kcal mol^{-1})	Residual amino acid interactions	
			H-bond	Hydrophobic/pi–cation/ pi–anion/pi–alkyl interactions	van der Walls interactions
6a	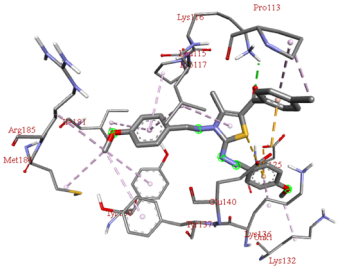	−9.6	LYS B:116	LYS B:132, LYS B:136, TYR B:137, PRO B:117, MET B:184, TYR B:160, ILE B:181, ARG B:185, LEU B:115, PRO B:113, GLU B:140, GLU B:125	—
6b	No interactions found	−7.2	—	—	—
6c	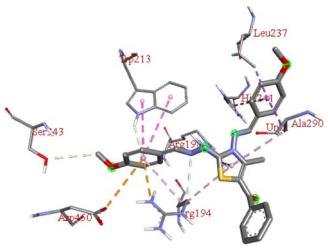	−9.1	ARG A:198	ASP A:450, ARG A:194, TRP A:213, SER A:343, HIS A:241, ALA A:290, LEU A:237	—
6d	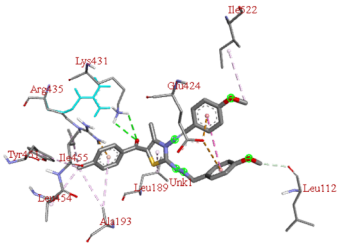	−7.9	LYS B:431	GLU B:424, ILE B:522, LEU B:112, ILE B:455, TYR B:451, LEU B:189, LEU B:454, ALA B:193, ARG B:435	—
6e	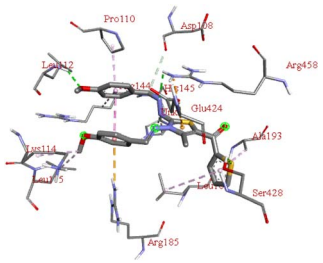	−7.5	LEU B:112, SER B:428, ARG B:458	GLU B:424, ARG B:185, LEU B:115, LYS B:114, ARG B:144, ASP B:108, PRO B:110, ALA B:193, HIS B:145, LEU B:189	—
6f	No interactions found	−7.0	—	—	—
6g	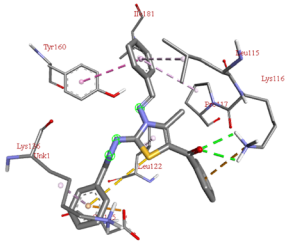	−9.2	LYS B:116	TYR B:160, ILE B:181, LEU B:115, PRO B:117, LEU B:122, LYS B:136, GLU B:125	—
6h	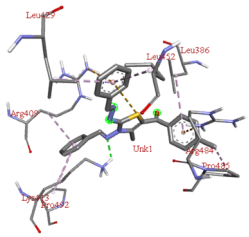	−8.7	LYS A:413	PRO A: 485, ARG A:484, LEU A:386, LEU A:452, LEU A:429, ARG A:409, PRO A:492	—

Table 7 (*Contd.*)

Cmpd	3D plot	Binding affinity (kcal mol^{-1})	Residual amino acid interactions		
			H-bond	Hydrophobic/pi–cation/ pi–anion/pi–alkyl interactions	van der Walls interactions
6i	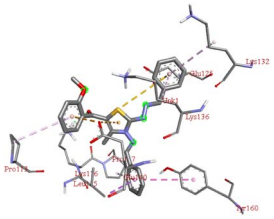	−8.8	LYS B:116	PRO B:113, LYS B:132, LYS B:136, GLU B:140, TYR B:160, LEU B:115, PRO B:117, GLU B:125	—
6j	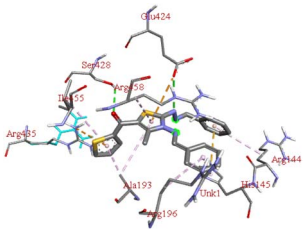	−7.8	GLU B:424, SER B:428	ARG B:144, ARG B:196, HIS B:145, ARG B:458, ALA B:193, ILE B:455, ARG B:435	—
6k	No interactions found	−7.4	—	—	—
6l	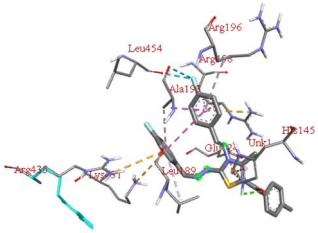	−9.2	HIS B:145	GLU B:424, LEU B:189, LYS B:431, ARG B:435, ALA B:193, LEU B:454, ARG B:458, ARG B:196	—
6m	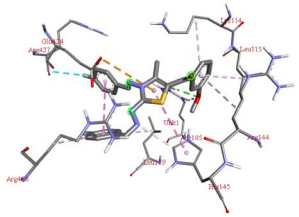	−8.3	ARG B:185	LYS B:114, LEU B:115, ARG B:144, HIS B:145, GLU B:424, ARG B:427, ARG B:458, LEU B: 189	—
6n	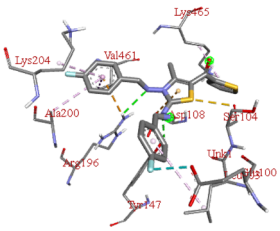	−7.6	ARG B:196, TYR B:147	LYS B:204, VAL B:461, ASP B:108, ALA B:200, LYS B: 465, SER B:104, LEU B:103, GLU B:100	—

2.2.9 UV-visible spectroscopy. UV-visible spectroscopy plays a significant role in identifying whether a ligand interacts with a protein or not by examining the perturbation in the microenvironment of the protein in the presence of a ligand. The absorption spectra of BSA protein are mainly characterized by two peaks, a strong band at 210 nm attributed to BSA protein framework and a weak band nearly at 280 nm accredited to the $\pi \rightarrow \pi^*$ transitions of aromatic amino acids *viz.*, Phenylalanine, Tryptophan and Tyrosine amino acids.[25] Any change in the microenvironment of protein in the presence of ligands results in the alteration of the absorption maximum thus confirming the interaction of ligands with protein. The absorption spectra of a fixed concentration of BSA protein in Phosphate Buffer saline (13 μM, pH 7.4) in the absence and presence of increasing concentrations of ligand **6a** (0–16 μM) were recorded at room temperature in the spectral range of 200–500 nm. Fig. 10a demonstrates a gradual increase in absorption maxima with a continuous rise in ligand concentration, demonstrating the preferred binding between ligand and BSA protein.

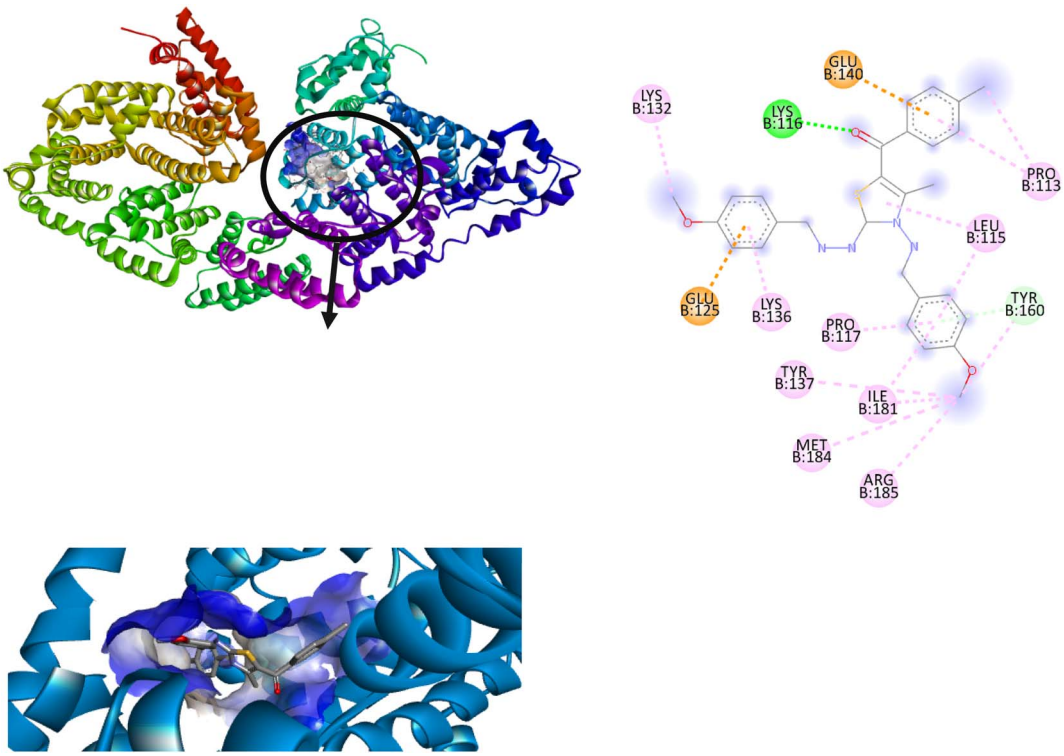

Fig. 9 2D and 3D poses of the interaction of ligand **6a** with BSA protein.

Furthermore, the method of continuous variation also acknowledged as Job's plot was employed to determine the binding stoichiometry of ligand and protein.[50] In this experiment, ten different solutions of BSA in Phosphate Buffer saline (13 μM, pH 7.4) and ligand **6a** were prepared by keeping the final concentration constant at 20 μM and absorption spectra of these solutions were monitored at 280 nm. A maximum at 0.5 was obtained from a graph between the mole fractions of ligand **6a** and absorbance at 280 nm indicating the 1 : 1 binding stoichiometry of ligand **6a** with BSA (Fig. 10b).

2.2.10 Fluorescence spectroscopy. The aromatic amino acids Phenylalanine (Phe), Tryptophan (Trp) and Tyrosine (Tyr) found in the BSA protein are extremely important because they have inherent fluorescence properties that aid in determining the various aspects of ligand–protein interactions. The ratio of the fluorescence intensities of Trp, Tyr, and Phe residues is 100 : 9 : 0.5, indicating that tryptophan residue is more important among these aromatic amino acids. As a result, the presence of any foreign ligand in the vicinity of these amino acids alters the intensity of emission of native BSA protein detected by the instrument.

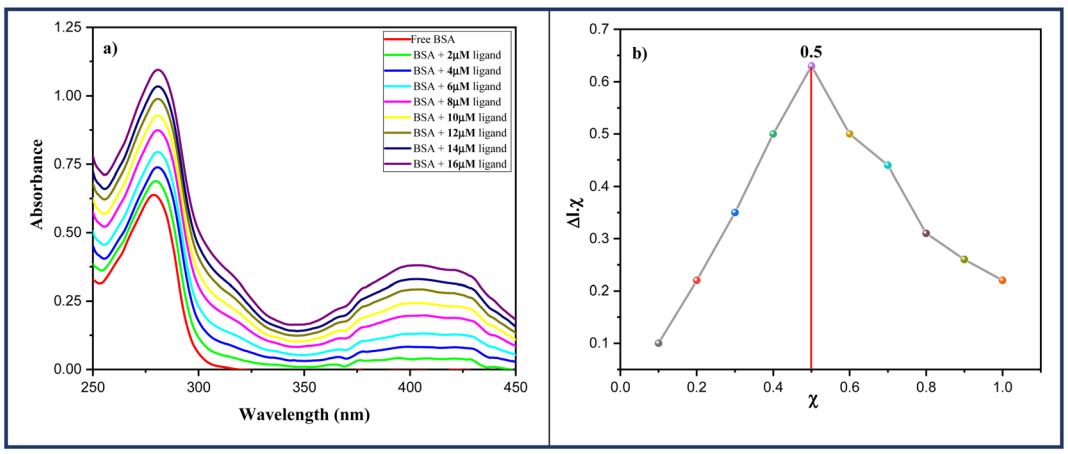

Fig. 10 (a) Absorption spectra of BSA protein (13 μM) in the absence and in the presence of an increasing ligand **6a** (0–16 μM) and (b) Job's plot for BSA-**6a** complex system.

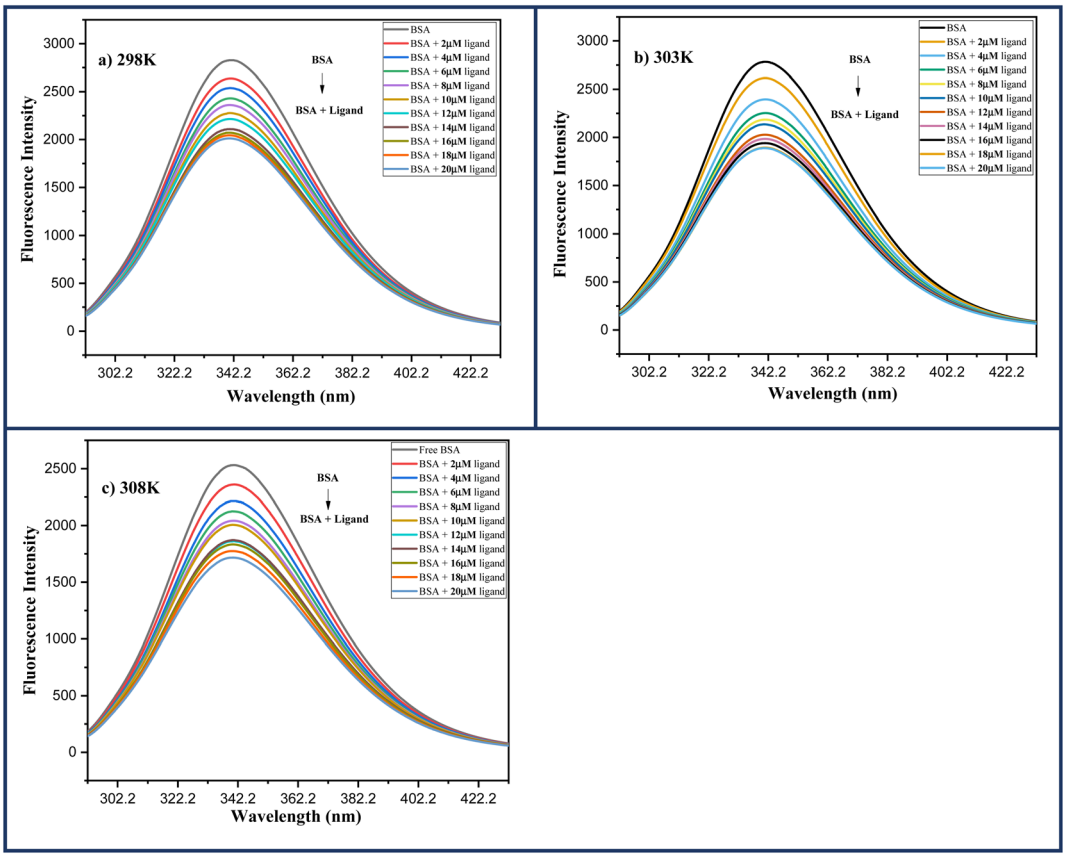

Fig. 11 Fluorescence spectra of BSA (13 μM) protein in the increasing ligand concentration **6a** (0–20 μM) at (a) 298 K; (b) 303 K; (c) 308 K.

In this experiment, a fixed concentration of BSA in Phosphate Buffer saline (13 μM, pH 7.4) was titrated with increasing ligand concentration **6a** (0–20 μM) and the data was collected in the spectral range of 300–500 nm while keeping the excitation wavelength (λ_{ex}) fixed at 290 nm. The emission maxima at 342 nm gradually decreased with increasing ligand concentration and was finally quenched at a higher concentration of ligand **6a**, indicating preferential binding of ligand **6a** with BSA protein. Further, the same procedure was carried out at three different temperatures: 298, 303, and 308 K with similar results Fig. 11.

Furthermore, a straight-line graph was obtained at three different temperatures: 298, 303, and 308 K using Stern–Volmer eqn (1) where the ratio of fluorescence intensity at 342 nm in the absence (F_o) and presence (F) of ligand **6a** was plotted against the increasing molar concentration [Q] of ligand **6a** by keeping

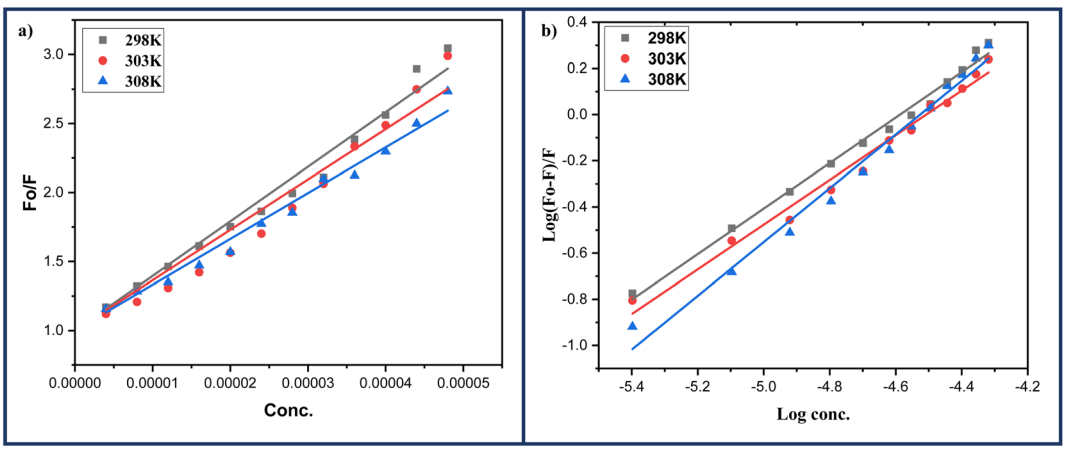

Fig. 12 (a) Stern–Volmer; (b) Scatchard's plots for the BSA-**6a** complex systems at varying three different temperatures: 298, 303 and 308 K respectively.

Table 8 Stern–Volmer constant (K_{sv}), quenching constant (K_q), binding constant (K_b), number of binding sites (n), Gibbs free energy ($\Delta G°$) and thermodynamic parameters ($\Delta H°$ & $\Delta S°$)

T (K)	$K_{sv} \times 10^4$ (M^{-1})	$K_q \times 10^{12}$ (M^{-1} s^{-1})	Log K_b	$K_b \times 10^4$ (M^{-1})	n	$\Delta G°$ (kJ mol^{-1})	$\Delta H°$ (kJ mol^{-1})	$\Delta S°$ (J mol^{-1} K^{-1})
298	(3.95 ± 0.09)	(3.95 ± 0.09)	5.27 ± 0.22	18.62	0.98 ± 0.02	−30.0	−156.1	−423.5
303	(3.64 ± 0.13)	(3.64 ± 0.13)	4.64 ± 0.19	4.36	0.96 ± 0.03	−26.9		
308	(3.31 ± 0.06)	(3.31 ± 0.06)	4.36 ± 0.18	2.29	1.16 ± 0.04	−25.7		

the intercept constant at 1 Fig. 12a. The quenching constants K_{sv} and K_q were calculated from this linear regression slope and are displayed in the Table 8. As the quenching constants K_{sv} and K_q show a decrement with the rise in temperature suggesting the static quenching mechanism is to be followed during the interaction process between ligand **6a** and BSA protein.

2.2.10.1 Identification of binding constant and number of binding sites. To determine the binding constant K_b and the number of binding sites n double-logarithmic Scatchard's eqn (2) was employed. A straight-line graph was obtained when the logarithmic ratio of the difference in fluorescence intensity of fluorophore in the absence and presence of quencher **6a** to the fluorescence intensity of fluorophore in the presence of quencher **6a** was plotted against the molar concentration of the quencher **6a** (Fig. 12b). The values of binding constant K_b and the number of binding sites n obtained from this linear regression at three temperatures: 298, 303, and 308 K are highlighted in the Table 8. The value of binding constant K_b comes out to be of the order 10^4 at all three temperatures indicative of moderate binding of ligand **6a** with BSA protein. Also, the number of binding sites was nearly found to be equal to 1 which is in great agreement with the outcomes of Job's plot.

Also, limit of detection (LOD) was calculated for each titration and the results are highlighted in Table S1.†

2.2.10.2 Identification of binding forces. Van't Hoff eqn (3) was utilized in order to identify the binding forces exhibited during the interaction process between ligand **6a** and BSA protein. It is evident (ESI Fig. S4†) that the straight-line regression attained from the plot of the logarithm of binding constant K_b and reciprocal of temperature ($1/T$). The thermodynamic parameters $\Delta H°$ & $\Delta S°$ calculated from the slope and the intercept of the plot respectively are displayed in the Table 8. The negative values of both the parameters ($\Delta H° = -156.1$ kJ mol^{-1} & $\Delta S° = -423.5$ J mol^{-1} K^{-1}), represents either van der Waals interaction or hydrogen bonding has occurred between ligand **6a** and BSA protein during the binding process.

Also, the change in Gibbs free energy ($\Delta G°$) was calculated at all three temperatures: 298, 303, and 308 K in order to identify the spontaneity of the binding process. The negative values of the $\Delta G°$ at all three temperatures indicate the spontaneity of the binding process between ligand **6a** and the BSA protein Table 8. Fig. S4† depicts the graphical representation of thermodynamic parameters $\Delta H°$, $\Delta S°$ and $\Delta G°$.

2.2.11 Binding site estimation: use of site markers. The crystallographic structure of BSA represents that it consists of three domains (I, II, III) where drugs can bind prudentially and each domain is further subdivided into subdomains (A and B). Among various binding sites present in BSA protein two are more important due to their explicit nature to accommodate a variety of ligands known as Sudlow's Site I and Sudlow's Site II. The former is situated in the subdomain IIA and is known to bind with drugs like oxyphenbutazone, phenylbutazone, warfarin and dansylamide whereas the latter is present inside the subdomain IIIA and shows better affinity towards drugs like diflunisal, diazepam, ibuprofen, indoxyl sulphate and dansylglycine.[51] Thus, in order to recognize the binding site for ligand **6a** on BSA, Ibuprofen and phenylbutazone were selected as the site marker ligands.

For the process, the fluorescence quenching experiments were carried out in which emission spectra of a pre-treated solution of BSA and site markers in 1 : 1 with increasing concentrations of ligand **6a** (0–20 μM) were recorded and displayed in (ESI Fig. S5†). The data so obtained was used to determine the binding constant K_b Table 9. As the value of the binding constant affected much in the case of phenylbutazone as compared to Ibuprofen hence ligand **6a** is supposed to bind in the same fashion as phenylbutazone does (Table 9). Thus, on the outcomes of site markers, it is concluded that ligand **6a** binds in Sudlow's Site I of BSA.

2.2.12 Circular dichroism. The far-UV circular dichroism is an important technique to explore the alteration in the secondary structure of biomacromolecules in the presence of foreign ligands. At room temperature, the far-UV circular dichroism spectrum of native BSA protein comprises two peaks in the negative region, one at 209 nm due to π–π* transition and the other at 221 nm attributed to n–π* transitions of the peptide bond arising due to the α-helicity of BSA protein.[52] The CD spectrum of BSA protein was obtained in the far UV region between 190 and 250 nm in the absence and presence of increasing amounts of ligand **6a** (0.2–1.0 μM). When native BSA protein was allowed to titrate with increasing concentration of ligand **6a** a shift in the negative minima at 221 nm was observed along with the disappearance of negative minima at 209 nm Fig. 13. Further increase in the concentration of ligand **6a** does not impart much effect on the spectrum. Thus, shifting of the

Table 9 Binding constants for the BSA-**6a** system in the presence of site markers at 298 K

System	K_b (M^{-1})
BSA + **6a**	18.62×10^4
BSA + IB + **6a**	16.81×10^4
BSA + PB + **6a**	6.48×10^4

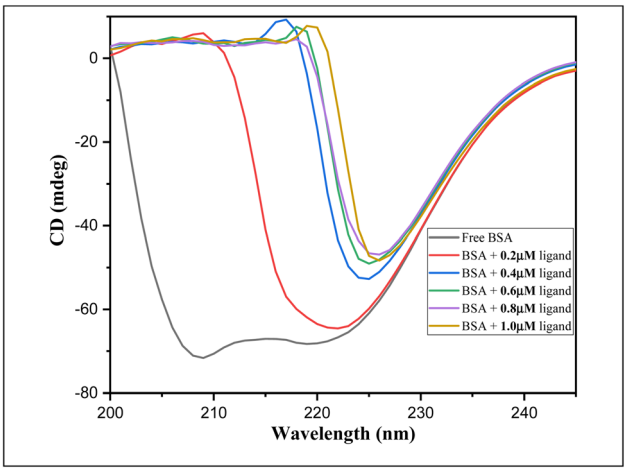

Fig. 13 CD spectra of BSA in the absence as well as in the presence of increasing concentration of ligand **6a**.

Table 10 Percentage helicity of the BSA protein in the presence of increasing concentration of **6a** (0.2–1.0 μM)

6a (μM)	0.2	0.4	0.6	0.8	1.0
% Helicity	**49.63**	**46.79**	**39.65**	**32.51**	**26.83**

CD spectrum in the presence of ligand **6a** confirms the binding potential of the synthesized 2,3-dihydrothiazole derivatives with BSA protein.

The CD results can be expressed in terms of mean residue ellipticity (MRE) (eqn (4))

$$\mathrm{MRE} = \frac{\mathrm{CD(obs)}}{C_p nl \times 10} \quad (4)$$

Here, observed CD is measured in meter degrees, C_p is the molar concentration of BSA, n is the number of amino acid residues (583 for BSA), and l is the path length (1 cm).

MRE can be used to calculate the α-helix content of BSA using following equation:

$$\alpha\text{-helix}(\%) = \frac{-[\mathrm{MRE}_{221} - 4000]}{[33\,000 - 4000]} \times 100 \quad (5)$$

where $[\theta]_{221}$ is the observed MRE value at 221 nm, 4000 is the MRE of the β-form and random coil conformation crosses at 221 nm and 33 000 is the MRE value of a pure α-helix at 221 nm.

Table 10 displayed the related decrease in ellipticity, indicative of helicity disruption or denaturation of protein structure by increasing concentration of ligand **6a**. The unfolding of the α-helix of protein occurs at the rate directly proportional to the concentration of **6a**. Thus, it can be concluded that at higher ligand concentration the BSA structure opens up *i.e.*, denaturation of protein happens.

3. Conclusion

In nutshell, regioselective synthesis of 5-aroyl-3-((arylidene) amino)-2-((arylidene)hydrazono)-4-methyl-2,3-dihydrothiazole derivatives **6a–n** has been successfully achieved in excellent yields by the one-pot reaction of thiocarbohydrazide **1** and aldehydes **2** with α-bromo-1,3-diketones **5** (generated *in situ* by the bromination of unsymmetrical 1,3-diketones **4(a–f)** with NBS) using white LED light (9 W) as a green energy source. Out of the two possible regioisomers the exact one was identified using multinuclear 2D-NMR [^{1}H–^{13}C] HMBC; [^{1}H–^{13}C] HMQC and [^{1}H–^{15}N] HMBC spectroscopic techniques. On the basis of *in silico* studies including molecular reactivity analysis, Lipinski rule and molecular docking 2,3-dihydrothiazole derivative **6a** was selected for binding studies with DNA and BSA biomolecules using UV-absorption spectroscopy, fluorescence and CD spectroscopy. The steady-state fluorescence supports the static mechanism that occurs during interactions of compound **6a** with DNA and BSA. The competitive displacement assay and circular dichroism analysis have also demonstrated compound **6a** to bind with DNA through grove binding mode. Furthermore, site-marker assay indicates ligand **6a** to bind with BSA at Sudlow's site I (in subdomain IIA). The theoretical outcomes of *in silico* studies agree very well with experimental *ex vivo* results. We hope that the outcomes of this study will help and motivate scientists to further explore the biological potential of 2,3-dihydrothiazole derivatives.

4. Experimental

4.1 General method of synthesis

1,3-Diketones and thiocarbohydrazide were prepared according to the literature procedure. Aldehydes and NBS were purchased commercially.

4.1.1 General method for the one-pot multicomponent regioselective synthesis of 5-aroyl-3-((arylidene)amino)-2-((arylidene)hydrazono)-4-methyl-2,3-dihydrothiazole derivatives (6a–n). The course of the reaction was initiated by the bromination of unsymmetrical 1,3-diketones **4** (1.0 eq.) using mild brominating agent NBS (1.0 eq.) under DCM stir at room temperature. Following successful bromination as indicated by the TLC, the excess solvent was eliminated from the reaction mixture at reduced pressure with the help of a rotatory evaporator. The resulting reaction mass was subjected to react with thiocarbohydrazide **1** (1.0 eq.) and aldehyde **2** (2.0 eq.) in EtOAc under irradiation of white LED light (9 W). The progress of the reaction was monitored repeatedly after every 5 minutes using TLC, indicating the complete consumption of the starting materials within 30–45 min. After the completion of the reaction, the left-over EtOAc was reduced under vacuum using a rotatory evaporator. The reaction mass so obtained was first neutralized with saturated $NaHCO_3$ solution to remove HBr produced during the progress of the reaction and then extracted several times with small portions of EtOAc. The organic layers were then combined and dried over anhydrous Na_2SO_4 and the solid thus obtained after the evaporation of solvent at room temperature was filtered, dried and recrystallized with EtOH to furnish the target thiazole derivatives **6a–n** in excellent yield 82–93%.

4.1.1.1 ***6a****. 5-(4′-chlorobenzoyl)-3-((4″-methoxybenzylidene) amino)-2-((4‴-methoxybenzylidene) hydrazono)- 4-methyl-2,3-*

dihydrothiazole. Yellow solid; M. pt. 176 °C; yield: 88%; IR (KBr) ν_{max} (cm^{-1}): 1592 (C=O), 1612 (C=N); ^1H NMR (400 MHz, $CDCl_3$) δ: 10.13 (s, 1H, 6-CH), 8.36 (s, 1H, 7-CH), 7.78–7.76 (d, 2H, ^3J = 8.8 Hz, Ph 2″, 6″-H), 7.74–7.70 (m, 4H, Ph 2′, 5′, 2‴, 6‴-H), 7.47–7.45 (d, 2H, ^3J = 8.4 Hz, Ph 3′, 6′-H), 6.99–6.97 (d, 2H, ^3J = 8.8 Hz, Ph 3″, 5″-H), 6.94–6.91 (d, 2H, ^3J = 8.8 Hz, Ph 3‴, 5‴-H), 3.88 (s, 3H, 4″-OCH_3), 3.85 (s, 3H, 4‴-OCH_3), 2.52 (s, 3H, 4-CH_3); ^{13}C NMR (100 MHz, $CDCl_3$) δ: 187.3, 163.4, 162.3, 161.6, 156.9, 155.3, 148.6, 138.4, 138.1, 130.0, 129.8, 129.6, 128.9, 127.5, 127.1, 114.4, 114.2, 111.3, 55.5, 55.4, 15.6; HRMS (EI) *m*/*z*: 519.1260 $[M+1]^+$, 521.1225 $[M+3]^+$ (3 : 1); Anal. Calcd. for $C_{27}H_{23}ClN_4O_3S$: C, 62.48; H, 4.47; N, 10.80% Found: C, 62.45; H, 4.45; N, 10.79%.

4.1.1.2 ***6b****. 5-(4′-bromobenzoyl)-3-((4″-methoxybenzylidene) amino)-2-((4‴-methoxybenzylidene) hydrazono)-4-methyl-2,3-dihydrothiazole.* Pale Yellow solid; M. pt. 179 °C; yield: 90%; IR (KBr) ν_{max} (cm^{-1}): 1594 (C=O), 1613 (C=N); ^1H NMR (400 MHz, $CDCl_3$) δ: 10.12 (s, 1H, 6-CH), 8.35 (s, 1H, 7-CH), 7.78–7.75 (d, 2H, ^3J = 8.8 Hz, Ph 2″, 6″-H), 7.72–7.70 (d, 2H, ^3J = 8.8 Hz, Ph 2‴, 6‴-H), 7.64–7.63 (d, 4H, ^3J = 4 Hz, Ph 2′, 3′, 5′, 6′-H), 6.98–6.96 (d, 2H, ^3J = 8.8 Hz, Ph 3″, 5″-H), 6.93–6.91 (d, 2H, ^3J = 8.8 Hz, Ph 3‴, 5‴-H), 3.87 (s, 3H, 4″-OCH_3), 3.84 (s, 3H, 4‴-OCH_3), 2.51 (s, 3H, 4-CH_3); ^{13}C NMR (100 MHz, $CDCl_3$) δ: 187.3, 163.4, 162.3, 161.6, 157.0, 155.3, 148.6, 138.5, 131.9, 130.1, 129.8, 129.6, 127.5, 127.1, 126.9, 114.4, 114.2, 111.3, 55.5, 55.4, 15.6; HRMS (EI) *m*/*z*: 563.0759 $[M+1]^+$, 565.0734 $[M+3]^+$ (1 : 1); Anal. Calcd. for $C_{27}H_{23}BrN_4O_3S$: C, 57.55; H, 4.11; N, 9.94% Found: C, 57.52; H, 4.09; N, 9.93%.

4.1.1.3 ***6c****. 5-benzoyl-3-((4″-methoxybenzylidene)amino)-2-((4‴-methoxybenzylidene)hydrazono)-4-methyl-2,3-dihydrothiazole.* Orange solid; M. pt. 165 °C; yield: 92%; IR (KBr) ν_{max} (cm^{-1}): 1596 (C=O), 1610 (C=N); ^1H NMR (400 MHz, $CDCl_3$) δ: 10.15 (s, 1H, 6-CH), 8.36 (s, 1H, 7-CH), 7.77–7.75 (m, 4H, Ph 2′, 6′, 2″, 6″-H), 7.72–7.70 (m, 2H, Ph 2‴, 6‴-H), 7.58–7.55 (m, 1H, Ph 4′-H), 7.50–7.46 (m, 2H, Ph 3′, 5′-H), 6.97–6.96 (d, 2H, ^3J = 4 Hz, Ph 3″, 5″-H), 6.92–6.91 (d, 2H, ^3J = 4 Hz, Ph 3‴, 5‴-H), 3.87 (s, 3H, 4″-OCH_3), 3.84 (s, 3H, 4‴-OCH_3), 2.47 (s, 3H, 4-CH_3); ^{13}C NMR (100 MHz, $CDCl_3$) δ: 188.7, 163.8, 162.2, 161.5, 156.7, 155.1, 148.1, 139.8, 132.1, 129.7, 129.5, 128.6, 128.5, 127.6, 127.2, 114.4, 114.2, 112.0, 55.5, 55.5, 15.7; HRMS (EI) *m*/*z*: 485.1697 $[M+1]^+$; Anal. Calcd. for $C_{27}H_{24}N_4O_3S$: C, 66.92; H, 4.91; N, 11.56% Found: C, 66.89; H, 4.90; N, 11.54%.

4.1.1.4 ***6d****. 3-((4″-methoxybenzylidene)amino)-2-((4‴-methoxybenzylidene)hydrazono)-4-methyl-5-(4′-methylbenzoyl)-2,3-dihydrothiazole.* Pale Yellow solid; M. pt. 188 °C; yield: 93%; IR (KBr) ν_{max} (cm^{-1}): 1591 (C=O), 1608 (C=N); ^1H NMR (400 MHz, $CDCl_3$) δ: 10.14 (s, 1H, 6-CH), 8.37 (s, 1H, 7-CH), 7.78–7.76 (d, 2H, ^3J = 8.8 Hz, Ph 2″, 6″-H), 7.73–7.68 (m, 4H, Ph 2′, 5′, 2‴, 6‴-H), 7.29–7.27 (d, 2H, ^3J = 8.4 Hz, Ph 3′, 6′-H), 6.98–6.96 (d, 2H, ^3J = 8.8 Hz, Ph 3″, 5″-H), 6.93–6.91 (d, 2H, ^3J = 8.8 Hz, Ph 3‴, 5‴-H), 3.88 (s, 3H, 4″-OCH_3), 3.85 (s, 3H, 4‴-OCH_3), 2.49 (s, 3H, 4-CH_3), 2.44 (s, 3H, 4′-CH_3); ^{13}C NMR (100 MHz, $CDCl_3$) δ: 188.4, 163.8, 162.2, 161.5, 154.9, 147.5, 142.9, 137.0, 129.7, 129.5, 129.2, 128.8, 127.7, 127.2, 114.4, 114.2, 55.5, 55.4, 21.7, 15.6; HRMS (EI) *m*/*z*: 499.1772 $[M+1]^+$; Anal. Calcd. for $C_{28}H_{26}N_4O_3S$: C, 67.45; H, 5.26; N, 11.24% Found: C, 67.43; H, 5.23; N, 11.23%.

4.1.1.5 ***6e****. 3-((4″-methoxybenzylidene)amino)-2-((4‴-methoxybenzylidene)hydrazono)-4-methyl-5-thienoyl-2,3-dihydrothiazole.* Black solid; M. pt. 175 °C; yield: 85%; IR (KBr) ν_{max} (cm^{-1}): 1586 (C=O), 1609 (C=N); ^1H NMR (400 MHz, $CDCl_3$) δ: 10.12 (s, 1H, 6-CH), 8.37 (s, 1H, 7-CH), 7.94–7.93 (dd, 1H, ^3J = 3.6 Hz, ^4J = 0.8 Hz, thienyl 3′-H), 7.79–7.77 (d, 2H, ^3J = 8.8 Hz, Ph 2″, 6″-H), 7.74–7.72 (d, 2H, Ph 2‴, 6‴-H), 7.67–7.66 (dd, 1H, ^3J = 4.8 Hz, ^5J = 0.8 Hz, thienyl 5′-H), 7.18–7.16 (dd, 1H, ^3J = 4.8 Hz, ^3J = 3.6 Hz, thienyl 4′-H), 6.99–6.96 (d, 2H, ^3J = 8.8 Hz, Ph 3″, 5″-H), 6.94–6.92 (d, 2H, ^3J = 8.8 Hz, Ph 3‴, 5‴-H), 3.88 (s, 3H, 4″-OCH_3), 3.85 (s, 3H, 4‴-OCH_3), 2.69 (s, 3H, 4-CH_3); ^{13}C NMR (100 MHz, $CDCl_3$) δ: 179.0, 163.1, 162.2, 161.5, 156.8, 155.0, 148.7, 145.2, 133.4, 132.5, 129.8, 129.5, 128.0, 127.6, 127.2, 114.4, 114.2, 109.5, 55.5, 55.4, 15.3; HRMS (EI) *m*/*z*: 491.1237 $[M+1]^+$; Anal. Calcd. for $C_{25}H_{22}N_4O_3S_2$: C, 61.21; H, 4.52; N, 11.42% Found: C, 61.19; H, 4.49; N, 11.40%.

4.1.1.6 ***6f****. 3-((benzylidene)amino)-2-(benzylidene)hydrazono)-5-(4′-bromobenzoyl)-4-methyl–2,3-dihydrothiazole.* Pale Yellow solid; M. pt. 176 °C; yield: 87%; IR (KBr) ν_{max} (cm^{-1}): 1597 (C=O), 1610 (C=N); ^1H NMR (400 MHz, $CDCl_3$) δ: 10.27 (s, 1H, 6-CH), 8.43 (s, 1H, 7-CH), 7.83–7.78 (m, 4H, Ph 2″, 6″, 2‴, 6‴-H), 7.65 (s, 4H, Ph 2′, 3′, 5′, 6′-H), 7.47–7.41 (m, 6H, Ph 3″, 4″, 5″, 3‴, 4‴, 5‴-H), 2.54 (s, 3H, 4-CH_3); ^{13}C NMR (100 MHz, $CDCl_3$) δ: 187.4, 164.3, 157.0, 155.9, 148.4, 138.4, 134.7, 134.5, 132.0, 131.4, 130.6, 130.2, 129.0, 128.8, 128.1, 128.1, 127.2, 111.8, 15.7; HRMS (EI) *m*/*z*: 503.0543 $[M+1]^+$, 505.0543 $[M+3]^+$ (1 : 1); Anal. Calcd. for $C_{25}H_{19}BrN_4OS$: C, 59.65; H, 3.80; N, 11.13% Found: C, 59.63; H, 3.79; N, 11.10%.

4.1.1.7 ***6g****. 5-benzoyl-3-((benzylidene)amino)-2-((benzylidene) hydrazono)-4-methyl-2,3-dihydrothiazole.* Yellow solid; M. pt. 150 °C; yield: 89%; IR (KBr) ν_{max} (cm^{-1}): 1597 (C=O), 1613 (C=N); ^1H NMR (400 MHz, $CDCl_3$) δ: 10.29 (s, 1H, 6-CH), 8.43 (s, 1H, 7-CH), 7.84–7.82 (m, 2H, Ph 2′, 6′-H), 7.79–7.76 (m, 4H, Ph 2″, 6″, 2‴, 6‴-H), 7.61–7.56 (m, 1H, Ph 4′-H), 7.52–7.49 (m, 2H, Ph 3′, 5′-H), 7.48–7.46 (m, 3H, Ph 3″, 4″, 5″-H), 7.42–7.39 (m, 3H, Ph 3‴, 4‴, 5‴-H), 2.50 (s, 3H, 4-CH_3); ^{13}C NMR (100 MHz, $CDCl_3$) δ: 188.8, 164.7, 156.7, 155.7, 147.8, 139.6, 134.7, 134.6, 132.3, 131.2, 130.5, 128.9, 128.8, 128.6, 128.6, 128.1, 128.0, 112.5, 15.7; HRMS (EI) *m*/*z*: 425.1441 $[M+1]^+$; Anal. Calcd. for $C_{25}H_{20}N_4OS$: C, 70.73; H, 4.75; N, 13.20% Found: C, 70.71; H, 4.72; N, 13.19%.

4.1.1.8 ***6h****. 3-((benzylidene)amino)-2-((benzylidene)hydrazono)-4-methyl-5-(4′-methylbenzoyl)-2,3-dihydrothiazole.* Pale Yellow solid; M. pt. 187 °C; yield: 92%; IR (KBr) ν_{max} (cm^{-1}): 1593 (C=O), 1605 (C=N); ^1H NMR (400 MHz, $CDCl_3$) δ: 10.29 (s, 1H, 6-CH), 8.43 (s, 1H, 7-CH), 7.84–7.77 (m, 4H, Ph 2″, 6″, 2‴, 6‴-H), 7.72–7.70 (d, 2H, ^3J = 8 Hz, Ph 2′, 6′-H), 7.47–7.46 (m, 3H, Ph 3″, 4″, 5″-H), 7.40–7.39 (m, 3H, Ph 3‴, 4‴, 5‴-H), 7.30–7.28 (d, 2H, ^3J = 8 Hz, Ph 3′, 5′-H), 2.51 (s, 3H, 4-CH_3), 2.45 (s, 3H, 4′-CH_3); ^{13}C NMR (100 MHz, $CDCl_3$) δ: 188.5, 156.6, 155.6, 143.2, 134.8, 134.7, 131.2, 130.4, 129.3, 128.9, 128.9, 128.8, 128.7, 128.1, 128.0, 21.8, 15.6; HRMS (EI) *m*/*z*: 439.1587 $[M+1]^+$; Anal. Calcd. for $C_{26}H_{22}N_4OS$: C, 71.21; H, 5.06; N, 12.78% Found: C, 71.20; H, 5.04; N, 12.75%.

4.1.1.9 ***6i****. 3-((benzylidene)amino)-2-((benzylidene)hydrazono)-5-(3′-methoxybenzoyl)-4-methyl–2,3-dihydrothiazole.* Pale Yellow solid; M. pt. 137 °C; yield: 84% IR (KBr) ν_{max} (cm^{-1}): 1599 (C=

O), 1610 (C=N); ^{1}H NMR (400 MHz, $CDCl_3$) δ: 10.29 (s, 1H, 6-CH), 8.44 (s, 1H, 7-CH), 7.87–7.75 (m, 4H, Ph 2″, 6″, 2‴, 6‴-H), 7.48–7.46 (m, 3H, Ph 5′, 4″, 4‴-H), 7.42–7.37 (m, 5H, Ph 6′, 3″, 5″, 3‴, 5‴-H), 7.28 (m, 1H, Ph 2′-H), 7.13–7.11 (m, 1H, Ph 4′-H), 3.88 (s, 3H, 3′-OCH_3), 2.51 (s, 3H, 4-CH_3); ^{13}C NMR (100 MHz, $CDCl_3$) δ: 188.5, 176.2, 159.8, 155.7, 143.0, 140.9, 134.6, 131.2, 130.4, 129.7, 128.9, 128.8, 128.1, 128.0, 126.0, 121.1, 118.8, 112.9, 55.6, 15.7; HRMS (EI) m/z: 455.1564 $[M+1]^+$; Anal. Calcd. for $C_{26}H_{22}N_4O_2S$: C, 68.70; H, 4.82; N, 12.33% Found: C,68.68; H, 4.81; N, 12.32%.

4.1.1.10 ***6j****. 3-((benzylidene)amino)-2-((benzylidene)hydrazono)-4-methyl-5-thienoyl-2,3dihydrothiazole.* Brown solid; M. pt. 171 °C; yield: 85%; IR (KBr) ν_{max} (cm^{-1}): 1587 (C=O), 1605 (C=N); ^{1}H NMR (400 MHz, $CDCl_3$) δ: 10.28 (s, 1H, 6-CH), 8.45 (s, 1H, 7-CH), 7.95 (s, 1H, thienyl 3′-H), 7.85–7.80 (m, 4H, Ph 2″, 6″, 2‴, 6‴-H), 7.69–7.68 (d, 1H, ^3J = 4 Hz, thienyl 5′-H), 7.48 (s, 3H, Ph 3″, 4″, 5″-H), 7.41 (s, 3H, Ph 3‴, 4‴, 5‴), 7.18 (m, 1H, thienyl 4′-H), 2.71 (s, 3H, 4-CH_3); ^{13}C NMR (100 MHz, $CDCl_3$) δ: 179.1, 164.0, 156.7, 155.7, 148.4, 145.0, 134.7, 134.6, 133.7, 132.7, 131.3, 130.5, 128.9, 128.8, 128.1, 128.0, 15.3; HRMS (EI) m/z: 431.0994 $[M+1]^+$; Anal. Calcd. for $C_{23}H_{18}N_4OS_2$: C, 64.16; H, 4.21; N, 13.01% Found: C, 64.14; H, 4.19; N, 13.00%.

4.1.1.11 ***6k****. 5-(4′-bromobenzoyl)-3-((4″-fluorobenzylidene) amino)-2-((4‴- benzylidene)hydrazono)-4-methyl-2,3-dihydrothiazole.* Orange solid; M. pt. 178 °C; yield: 88%; IR (KBr) ν_{max} (cm^{-1}): 1586 (C=O, 1609 (C=N); ^{1}H NMR (400 MHz, $CDCl_3$) δ: 10.24 (s, 1H, 6-CH), 8.38 (s, 1H, 7-CH), 7.84–7.80 (m, 2H, Ph 2‴, 6‴-H), 7.78–7.74 (m, 2H, Ph 2″, 6″-H), 7.65–7.64 (d, 4H, ^3J = 4 Hz, Ph 2′, 3′, 5′, 6′-H), 7.18–7.14 (m, 2H, Ph 3‴, 5‴-H), 7.12–7.08 (m, 2H, Ph 3″, 5″-H), 2.53 (s, 3H, 4-CH_3); ^{13}C NMR (100 MHz, $CDCl_3$) δ: 187.4, 165.9, 165.5, 164.3, 163.4, 155.7, 154.6, 148.1, 138.2, 131.9, 130.9, 130.9, 130.7, 130.7, 130.2, 130.1, 130.0, 129.9, 129.8, 127.2, 116.3, 116.1, 115.9, 111.8, 15.6; ^{19}F NMR (300 MHz, $CDCl_3$) δ: −107.88, −109.16; HRMS (EI) m/z: 539.0349 $[M+1]^+$, 541.0322 $[M+3]^+$ (1 : 1); Anal. Calcd. for $C_{25}H_{17}BrF_2N_4OS$: C, 55.67; H, 3.18; N, 10.39% Found: C, 55.65; H, 3.15; N, 10.38%.

4.1.1.12 ***6l****. 3-((4″-fluorobenzylidene)amino)-2-((4‴-fluorobenzylidene)hydrazono)-4-methyl-5-(4′-methylbenzoyl)-2,3-dihydrothiazole.* Yellow solid; M. pt. 151 °C; yield: 87%; IR (KBr) ν_{max} (cm^{-1}): 1598 (C=O), 1615 (C=N); ^{1}H NMR (400 MHz, $CDCl_3$) δ: 10.25 (s, 1H, 6-CH), 8.38 (s, 1H, 7-CH), 7.83–7.79 (m, 2H, Ph 2‴, 6‴-H), 7.77–7.74 (m, 2H, Ph 2″, 6″-H), 7.61–7.59 (d, 2H, ^3J = 8 Hz, Ph 2′, 6′-H), 7.30–7.28 (d, 2H, ^3J = 8 Hz, Ph 3′, 5′-H), 7.17–7.13 (m, 2H, Ph 3‴, 5‴-H), 7.11–7.06 (m, 2H, Ph 3″, 5″-H), 2.49 (s, 3H, 4-CH_3), 2.45 (s, 3H, 4′-CH_3); ^{13}C NMR (100 MHz, $CDCl_3$) δ: 188.4, 165.8, 165.4, 164.7, 163.3, 162.9, 155.2, 154.2, 147.1, 143.2, 136.7, 131.0, 131.0, 130.9, 130.8, 130.0, 129.9, 129.8, 129.8, 129.3, 128.9, 116.2, 116.0, 115.8, 112.5, 21.8, 15.6; ^{19}F NMR (300 MHz, $CDCl_3$) δ: −108.20, −109.43; HRMS (EI) m/z: 475.1407 $[M+1]^+$; Anal. Calcd. for $C_{26}H_{20}F_2N_4OS$: C, 65.81; H, 4.25; N, 11.81% Found: C, 65.79; H, 4.22; N, 11.80%.

4.1.1.13 ***6m****. 3-((4″-fluorobenzylidene)amino)-2-((4‴-fluorobenzylidene)hydrazono)-5-(3′-methoxy benzoyl)-4-methyl–2,3-dihydrothiazole.* Pale Yellow solid; M. pt. 158 °C; yield: 83%; IR (KBr) ν_{max} (cm^{-1}): 1590 (C=O), 1603 (C=N); ^{1}H NMR (400 MHz, $CDCl_3$) δ: 10.24 (s, 1H, 6-CH), 8.39 (s, 1H, 7-CH), 7.83–7.80 (m, 2H, Ph 2‴, 6‴-H), 7.78–7.74 (m, 2H, Ph 2″, 6″-H), 7.42–7.38 (t, 1H, ^3J = 8 Hz, Ph 5′-H), 7.36–7.34 (m, 1H, Ph 6′-H), 7.27 (m, 1H, Ph 2′-H), 7.17–7.07 (m, 5H, Ph 4′, 3″, 5″, 3‴, 5‴-H), 3.87 (s, 3H, 3′-OCH_3), 2.68 (s, 3H, 4-CH_3); ^{13}C NMR (100 MHz, $CDCl_3$) δ: 188.4, 165.9, 165.4, 164.7, 163.4, 162.95, 159.8, 155.6, 154.3, 147.6, 140.8, 131.0, 130.9, 130.8, 130.7, 130.0, 129.9, 129.9, 129.8, 129.7, 121.0, 118.8, 116.3, 116.0, 115.8, 113.0, 112.6, 55.6, 15.6; ^{19}F NMR (300 MHz, $CDCl_3$) δ: −108.03, −109.34; HRMS (EI) m/z: 491.1378 $[M+1]^+$; Anal. Calcd. for $C_{26}H_{20}F_2N_4O_2S$: C, 63.66; H, 4.11; N, 11.42% Found: C, 63.64; H, 4.09; N, 11.41%.

4.1.1.14 ***6n****. 3-((4″-fluorobenzylidene)amino)-2-((4‴-fluorobenzylidene)hydrazono)-4-methyl-5-thienoyl −2,3-dihydrothiazole.* Brown solid; M. pt. 175 °C; yield: 82%; IR (KBr) ν_{max} (cm^{-1}): 1583 (C=O), 1606 (C=N); ^{1}H NMR (400 MHz, $CDCl_3$) δ: 10.23 (s, 1H, 6-CH), 8.38 (s, 1H, 7-CH), 7.93–7.92 (d, 1H, ^3J = 4 Hz, thienyl 3′-H), 7.84–7.80 (m, 2H, Ph 2‴, 6‴-H), 7.79–7.75 (m, 2H, Ph 2″, 6″-H), 7.69–7.68 (d, 1H, ^3J = 4 Hz, thienyl 5′-H), 7.18–7.08 (m, 5H, thienyl 4′-H, Ph 3″, 5″, 3‴, 5‴-H), 2.68 (s, 3H, 4-CH_3); ^{13}C NMR (100 MHz, $CDCl_3$) δ: 179.0, 165.9, 165.4, 164.0, 163.4, 162.9, 155.3, 154.3, 148.2, 144.9, 133.7, 132.7, 131.0, 130.95 130.8, 130.8, 130.0, 129.9, 129.9, 129.8, 128.0, 116.3, 116.1, 116.0, 115.8, 110.0, 15.3; ^{19}F NMR (300 MHz, $CDCl_3$) δ: −108.07, −109.30; HRMS (EI) m/z: 467.0804 $[M+1]^+$; Anal. Calcd. for $C_{23}H_{16}F_2N_4OS_2$: C, 59.22; H, 3.46; N, 12.01% Found: C, 59.20; H, 3.45; N, 11.99%.

Data availability

Data for this article, including experimental data, (^{1}H, ^{13}C, [^{1}H–^{13}C] HMBC; [^{1}H–^{13}C] HMQC and [^{1}H–^{15}N] HMBC) for final compounds, Van't Hoff plot, CD spectrum for DNA, fluorescence spectra of BSA-IB and BSA-PB complexes and a general experimental section for both synthesis and binding studies have been included as part of the ESI.†

Conflicts of interest

The authors declare no competing interest.

Acknowledgements

We are highly thankful to Haryana State Council for Science, Innovation and Technology (HSCSIT), Panchkula for financial assistance to Naman Jain as project fellow.

References

1 K. Chen, X. Yao, T. Tang, L. M. Chen, C. Xiao, J. Y. Wang, H. F. Chen, Z. X. Jiang, Y. Liu and X. Zheng, Thiazole-based and thiazolidine-based protein tyrosine phosphatase 1B inhibitors as potential anti-diabetes agents, *Med. Chem. Res.*, 2021, **30**, 519–534.

2 T. I. de Santana, M. de O. Barbosa, P. A. T. de M. Gomes, A. C. N. da Cruz, T. G. da Silva and A. C. L. Leite, Synthesis, anticancer activity and mechanism of action of new thiazole derivatives, *Eur. J. Med. Chem.*, 2018, **144**, 874–886.

3 J. Jacob P and S. L. Manju, Identification and development of thiazole leads as COX-2/5-LOX inhibitors through in-vitro and in-vivo biological evaluation for anti-inflammatory activity, *Bioorg. Chem.*, 2020, **100**, 103882.
4 K. K. Bansal, J. K. Bhardwaj, P. Saraf, V. K. Thakur and P. C. Sharma, Synthesis of thiazole clubbed pyrazole derivatives as apoptosis inducers and anti-infective agents, *Mater. Today Chem.*, 2020, **17**, 100335.
5 G. Kumar and N. P. Singh, Synthesis, anti-inflammatory and analgesic evaluation of thiazole/oxazole substituted benzothiazole derivatives, *Bioorg. Chem.*, 2021, **107**, 104608.
6 I. Althagafi, N. El-Metwaly and T. A. Farghaly, New series of thiazole derivatives: synthesis, structural elucidation, antimicrobial activity, molecular modeling and MOE docking, *Molecules*, 2019, **24**, 1–23.
7 A. Rauf, M. K. Kashif, B. A. Saeed, N. A. Al-Masoudi and S. Hameed, Synthesis, anti-HIV activity, molecular modeling study and QSAR of new designed 2-(2-arylidenehydrazinyl)-4-arylthiazoles, *J. Mol. Struct.*, 2019, **1198**, 126866.
8 M. Mic, A. Pîrnău, C. G. Floare, G. Marc, A. H. Franchini, O. Oniga, L. Vlase and M. Bogdan, Synthesis and molecular interaction study of a diphenolic hidrazinyl-thiazole compound with strong antioxidant and antiradical activity with HSA, *J. Mol. Struct.*, 2021, **1244**, 7–10.
9 S. Sahu, S. K. Ghosh, P. Gahtori, U. Pratap Singh, D. R. Bhattacharyya and H. R. Bhat, In silico ADMET study, docking, synthesis and antimalarial evaluation of thiazole-1,3,5-triazine derivatives as Pf-DHFR inhibitor, *Pharmacol. Rep.*, 2019, **71**, 762–767.
10 Y. A. Ammar, S. M. A. A. El-Hafez, S. A. Hessein, A. M. Ali, A. A. Askar and A. Ragab, One-pot strategy for thiazole tethered 7-ethoxy quinoline hybrids: synthesis and potential antimicrobial agents as dihydrofolate reductase (DHFR) inhibitors with molecular docking study, *J. Mol. Struct.*, 2021, **1242**, 130748.
11 C. P. Suffridge, L. M. Bolaños, K. Bergauer, A. Z. Worden, J. Morré, M. J. Behrenfeld and S. J. Giovannoni, Exploring Vitamin B1 Cycling and Its Connections to the Microbial Community in the North Atlantic Ocean, *Front. Mar. Sci.*, 2020, **7**, 1–16.
12 E. Bugiardini, S. Pope, R. G. Feichtinger, O. V. Poole, A. M. Pittman, C. E. Woodward, S. Heales, R. Quinlivan, H. Houlden, J. A. Mayr, M. G. Hanna and R. D. S. Pitceathly, Utility of whole blood thiamine pyrophosphate evaluation in TPK1-related diseases, *J. Clin. Med.*, 2019, **8**, 991.
13 H. Cheng, H. Huang and G. Huang, Synthesis and antitumor activity of epothilone B, *Eur. J. Med. Chem.*, 2018, **157**, 925–934.
14 R. J. Morrison, F. W. Van Der Mei, F. Romiti and A. H. Hoveyda, A Catalytic Approach for Enantioselective Synthesis of Homoallylic Alcohols Bearing a Z-Alkenyl Chloride or Trifluoromethyl Group. A Concise and Protecting Group-Free Synthesis of Mycothiazole, *J. Am. Chem. Soc.*, 2020, **142**, 436–447.
15 Y. J. Luo, B. L. Wang, S. B. Kou, Z. Y. Lin, K. L. Zhou, Y. Y. Lou and J. H. Shi, Assessment on the binding characteristics of dasatinib, a tyrosine kinase inhibitor to calf thymus DNA: insights from multi-spectroscopic methodologies and molecular docking as well as DFT calculation, *J. Biomol. Struct. Dyn.*, 2020, **38**, 4210–4220.
16 A. K. Das, S. I. Druzhinin, H. Ihmels, M. Müller and H. Schönherr, Colorimetric and Fluorimetric DNA Detection with a Hydroxystyryl–Quinolizinium Photoacid and Its Application for Cell Imaging, *Chem. –Eur. J.*, 2019, **25**, 12703–12707.
17 P. Sangeetha, C. Sankar and K. Tharini, New thiazoldinone substituted 2,6-diarypiperidin-4-one: synthesis, crystal structure, spectral characterization, binding mode with calf thymus DNA, *J. Mol. Struct.*, 2019, **1198**, 126899.
18 J. Wang, M. F. Ansari and C. H. Zhou, Identification of Unique Quinazolone Thiazoles as Novel Structural Scaffolds for Potential Gram-Negative Bacterial Conquerors, *J. Med. Chem.*, 2021, **64**, 7630–7645.
19 M. H. El-Wakil, A. F. El-Yazbi, H. M. A. Ashour, M. A. Khalil, K. A. Ismail and I. M. Labouta, Discovery of a novel DNA binding agent via design and synthesis of new thiazole hybrids and fused 1,2,4-triazines as potential antitumor agents: computational, spectrometric and in silico studies, *Bioorg. Chem.*, 2019, **90**, 103089.
20 T. A. Farghaly, A. M. Abo Alnaja, H. A. El-Ghamry and M. R. Shaaban, Synthesis and DNA binding of novel bioactive thiazole derivatives pendent to N-phenylmorpholine moiety, *Bioorg. Chem.*, 2020, **102**, 104103.
21 J. E. F. Alves, J. F. de Oliveira, T. R. C. de Lima Souza, R. O. de Moura, L. B. de Carvalho Júnior, M. do C. Alves de Lima and S. M. V. de Almeida, Novel indole-thiazole and indole-thiazolidinone derivatives as DNA groove binders, *Int. J. Biol. Macromol.*, 2021, **170**, 622–635.
22 P. F. da S. Santos-Junior, I. J. dos S. Nascimento, E. C. D. da Silva, K. L. C. Monteiro, J. D. de Freitas, S. de Lima Lins, T. M. S. Maciel, B. C. Cavalcanti, J. de B. José de, F. C. de Abreu, I. M. Figueiredo, J. C. C. Santos, C. do Ó. Pessoa, E. F. da Silva-Júnior, J. X. de Araújo-Júnior and T. M. de Aquino, Synthesis of hybrids thiazole-quinoline, thiazole-indole and their analogs:in vitroanti-proliferative effects on cancer cell lines, DNA binding properties and molecular modeling, *New J. Chem.*, 2021, **45**, 13847–13859.
23 S. Eryılmaz, E. Türk Çelikoğlu, Ö. İdil, E. İnkaya, Z. Kozak, E. Mısır and M. Gül, Derivatives of pyridine and thiazole hybrid: synthesis, DFT, biological evaluation via antimicrobial and DNA cleavage activity, *Bioorg. Chem.*, 2020, **95**, 103476.
24 X. Su, L. Wang, Y. Xu, L. Dong and H. Lu, Study on the binding mechanism of thiamethoxam with three model proteins:spectroscopic studies and theoretical simulations, *Ecotoxicol. Environ. Saf.*, 2021, **207**, 111280.
25 B. C. Yallur, U. Katrahalli, P. M. Krishna and M. D. Hadagali, BSA binding and antibacterial studies of newly synthesized 5,6-Dihydroimidazo[2,1-b]thiazole-2-carbaldehyde, *Spectrochim. Acta, Part A*, 2019, **222**, 117192.

26 R. Aggarwal, M. Hooda, N. Jain, D. Sanz, R. M. Claramunt, B. Twamley and I. Rozas, An efficient, one-pot, regioselective synthesis of 2-aryl/hetaryl-4-methyl-5-acylthiazoles under solvent-free conditions, *J. Sulfur Chem.*, 2022, **43**, 12–21.

27 R. Aggarwal, M. Hooda, P. Kumar and G. Sumran, Solvent-free, Silica Catalyzed Intriguing Conversion of 3-Hydrazonobutan-2-one Oxime into Biacetyl Bis-hydrazone Schiff Bases, *Lett. Org. Chem.*, 2021, **18**, 532–537.

28 R. Aggarwal, M. Hooda, P. Kumar, S. Kumar, S. Singh and R. Chandra, An expeditious on-water regioselective synthesis of novel arylidene-hydrazinyl-thiazoles as DNA targeting agents, *Bioorg. Chem.*, 2023, **136**, 106524.

29 R. Aggarwal, M. Hooda, P. Kumar and M. C. Torralba, Visible-light-mediated regioselective synthesis of novel thiazolo[3,2-: B] [1,2,4]triazoles: advantageous synthetic application of aqueous conditions, *Org. Biomol. Chem.*, 2022, **20**, 584–595.

30 R. Aggarwal, S. Kumar and G. Singh, Multi-component reaction to access a library of polyfunctionally substituted 4 , 7- dihydropyrazolo [3 , 4- b] pyridines, *Synth. Commun.*, 2019, 1–13.

31 R. Aggarwal, One-pot synthesis and in vitro bioactivity of novel 4-aminopyrazolo [3 , 4- b] pyridine derivatives as potential antimicrobial compounds, *Med. Chem. Res.*, 2024, **33**, 117–126.

32 R. Aggarwal, N. Jain, S. Sharma, P. Kumar, G. P. Dubey, H. Chugh and R. Chandra, Visible-light driven regioselective synthesis, characterization and binding studies of 2-aroyl-3-methyl-6,7-dihydro-5H-thiazolo[3,2-a] pyrimidines with DNA and BSA using biophysical and computational techniques, *Sci. Rep.*, 2021, **11**, 1–18.

33 R. Aggarwal, M. Hooda, P. Kumar, N. Jain, G. P. Dubey, H. Chugh and R. Chandra, Visible-Light-Prompted Synthesis and Binding Studies of 5,6-Dihydroimidazo[2,1-b]thiazoles with BSA and DNA Using Biophysical and Computational Methods, *J. Org. Chem.*, 2022, **87**, 3952–3966.

34 R. Aggarwal, N. Jain, G. P. Dubey, S. Singh and R. Chandra, Visible Light-Prompted Regioselective Synthesis of Novel 5-Aroyl/hetaroyl-2′,4-dimethyl-2,4′-bithiazoles as DNA- and BSA-Targeting Agents, *Biomacromolecules*, 2023, **24**, 4798–4818.

35 R. Aggarwal and M. Hooda, Visible-light promoted serendipitous synthesis of 3,5-diaryl-1,2,4-thiadiazoles via oxidative dimerization of thiobenzamides, *J. Sulfur Chem.*, 2022, **43**, 242–251.

36 R. Aggarwal, S. Sharma, M. Hooda, D. Sanz, R. M. Claramunt, B. Twamley and I. Rozas, Visible-light mediated regioselective approach towards synthesis of 7-aroyl-6-methyl-[1,2,4]triazolo[3,4-b][1,3,4]thiadiazines, *Tetrahedron*, 2019, **75**, 130728.

37 S. Mamidala, S. R. Peddi, R. K. Aravilli, P. C. Jilloju, V. Manga and R. R. Vedula, Microwave irradiated one pot, three component synthesis of a new series of hybrid coumarin based thiazoles: antibacterial evaluation and molecular docking studies, *J. Mol. Struct.*, 2021, **1225**, 129114.

38 R. Raveesha, A. M. Anusuya, A. V. Raghu, K. Yogesh Kumar, M. G. Dileep Kumar, S. B. Benaka Prasad and M. K. Prashanth, Visible-light-mediated regioselective synthesis of novel thiazolo[3,2-: B] [1,2,4]triazoles: advantageous synthetic application of aqueous conditions, *Comput. Toxicol.*, 2022, **21**, 100202.

39 V. K. Choudhary, A. K. Bhatt, D. Dash and N. Sharma, DFT calculations on molecular structures, HOMO–LUMO study, reactivity descriptors and spectral analyses of newly synthesized diorganotin(IV) 2-chloridophenylacetohydroxamate complexes, *J. Comput. Chem.*, 2019, **40**, 2354–2363.

40 J. Haribabu, V. Garisetti, R. E. Malekshah, S. Srividya, D. Gayathri, N. Bhuvanesh, R. V. Mangalaraja, C. Echeverria and R. Karvembu, Design and synthesis of heterocyclic azole based bioactive compounds: molecular structures, quantum simulation, and mechanistic studies through docking as multi-target inhibitors of SARS-CoV-2 and cytotoxicity, *J. Mol. Struct.*, 2022, **1250**, 131782.

41 R. Raveesha, A. M. Anusuya, A. V. Raghu, K. Yogesh Kumar, M. G. Dileep Kumar, S. B. Benaka Prasad and M. K. Prashanth, Discovery of novel JAK2 and EGFR inhibitors from a series of thiazole-based chalcone derivatives, *Comput. Toxicol.*, 2022, **21**, 100202.

42 A. B. Umar, A. Uzairu, S. Uba and G. A. Shallangwa, In silico Studies of some potential anti-cancer agents on M19-MEL cell line, *Moroccan J. Chem.*, 2021, **9**, 260–273.

43 H. Mahaki, H. Tanzadehpanah, O. K. Abou-Zied, N. H. Moghadam, A. Bahmani, S. Salehzadeh, D. Dastan and M. Saidijam, Cytotoxicity and antioxidant activity of Kamolonol acetate from Ferula pseudalliacea, and studying its interactions with calf thymus DNA (ct-DNA) and human serum albumin (HSA) by spectroscopic and molecular docking techniques, *Process Biochem.*, 2019, **79**, 203–213.

44 Z. Nan, C. Hao, X. Ye, Y. Feng and R. Sun, Interaction of graphene oxide with bovine serum albumin: a fluorescence quenching study, *Spectrochim. Acta, Part A*, 2019, **210**, 348–354.

45 M. Szymańska, M. Insińska-Rak, G. Dutkiewicz, G. N. Roviello, M. A. Fik-Jaskółka and V. Patroniak, Thiophene-benzothiazole dyad ligand and its Ag(I) complex – Synthesis, characterization, interactions with DNA and BSA, *J. Mol. Liq.*, 2020, **319**, 1–10.

46 S. Singhal, P. Khanna and L. Khanna, Synthesis, DFT studies, molecular docking, antimicrobial screening and UV fluorescence studies on ct-DNA for novel Schiff bases of 2-(1-aminobenzyl) benzimidazole, *Heliyon*, 2019, **5**, e02596.

47 K. P. Thakor, M. V. Lunagariya, B. S. Bhatt and M. N. Patel, Fluorescence and absorption studies of DNA–Pd(II) complex interaction: synthesis, spectroanalytical investigations and biological activities, *Luminescence*, 2019, **34**, 113–124.

48 S. Kumar and M. S. Nair, Deciphering the interaction of flavones with calf thymus DNA and octamer DNA sequence (CCAATTGG)2, *RSC Adv.*, 2021, **11**, 29354–29371.

49 S. Salehzadeh, F. Hajibabaei, N. H. Moghadam, S. Sharifinia, S. Khazalpour and R. Golbedaghi, Binding Studies of Isoxsuprine Hydrochloride to Calf Thymus DNA Using Multispectroscopic and Molecular Docking Techniques, *J. Fluoresc.*, 2018, **28**, 195–206.

50 P. R. Patlolla, N. Desai, S. Gupta and B. Datta, Interaction of a dimeric carbocyanine dye aggregate with bovine serum albumin in non-aggregated and aggregated forms, *Spectrochim. Acta, Part A*, 2019, **209**, 256–263.

51 K. Karami, N. Jamshidian and M. Zakariazadeh, Synthesis, characterization and molecular docking of new C,N-palladacycles containing pyridinium-derived ligands: DNA and BSA interaction studies and evaluation as anti-tumor agents, *Appl. Organomet. Chem.*, 2019, **33**, 3747–3751.

52 J. Gu, S. Zheng, H. Zhao and T. Sun, Investigation on the interaction between triclosan and bovine serum albumin by spectroscopic methods, *J. Environ. Sci. Health, Part B*, 2020, **55**, 52–59.